LASER & PHOTONICS REVIEWS

Laser Photonics Rev. **6**, No. 4, 526–548 (2012) / **DOI** 10.1002/lpor.201100022

Abstract An overview is presented of recently developed light-mediated methods for ferroelectric domain engineering of lithium niobate single crystals. These methods include *light-assisted poling*, *UV laser-induced inhibition of poling*, and *all-optical poling*. In addition to the primary application of ferroelectric domain patterns, namely the realization of non-linear optical devices, the ability of transferring a domain pattern into a topographical structure by domain selective etching allows also for surface structuring of lithium niobate. This intertwining between ferroelectric domain patterns and surface topography has been used to fabricate exquisite micro-structures based on unusual domains generated purposefully by these light-mediated methods.

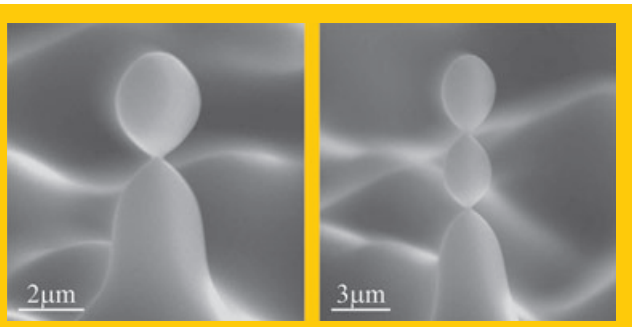

Light-mediated ferroelectric domain engineering and micro-structuring of lithium niobate crystals

Charlie Y. J. Ying[1,*], Alistair C. Muir[2], Christopher E. Valdivia[1,3], Hendrik Steigerwald[4], Collin L. Sones[1], Robert W. Eason[1], Elisabeth Soergel[4], and Sakellaris Mailis[1]

1. Introduction

As the level of complexity and sophistication in modern technological applications increases, the level of material processing which is required has to follow suit. A good example that demonstrates this principle is the silicon-based microelectronics industry where further miniaturization constantly requires again and again new technological solutions. A similar route is being followed by the photonics industry with the obvious example of optical fibre communication: the demand for ever higher data transmission rates requires even more complex optical devices to process them. In this research effort several optical materials, apart from silica, have been put to the test and one of them is lithium niobate. This material is already playing an important role in today's photonics industry and could become a suitable platform material for advanced integrated photonic applications [1].

Lithium niobate (LN) [2] is a ferroelectric crystal which supports two distinct orientations of the spontaneous polarization along its z-axis. LN belongs to the $3m$ point group, therefore, exhibiting three-fold rotation symmetry with the three mirror planes (yz planes) that are 60° apart interacting with the rotation z-axis. As a consequence of being ferroelectric, the crystal is also piezoelectric, pyroelectric, and electro-optic. Most importantly for photonic applications, LN exhibits a substantial optical nonlinearity which is essential, for instance, for ultrafast Mach-Zehnder modulators that are now commercially used in optical telecommunication networks reaching modulation rates up to 100 Gbit s^{-1} [3, 4]. Efficient wavelength converters using quasi-phase matching (QPM) in periodically poled LN crystals (PPLN) also make use of the large nonlinear coefficient [5] and similarly via the electro-optic effect for Bragg deflectors [6]. But domain patterns have also proven to be hugely useful for surface or bulk micro-structuring of LN using domain selective etching [7, 8].

Ferroelectric domain inversion can be achieved by applying an external electric field exceeding the coercive field E_c along the polar direction of the crystal, a process referred to as electric field poling (EFP). E_c varies for LN crystals of different compositions by one order of magnitude (see also Table 1). In order to accomplish spatially selective ferroelectric domain inversion in LN via EFP, one must locally alter either the E-field or E_c. Modulation of the E-field can be achieved, e. g., by micro-structuring of the electrodes [9] or by applying a micro-structured dielectric layer onto the crystal surface in conjunction with liquid electrodes [10]. Local modification of E_c has for instance been realized by spatially selective proton exchange [11]. Although EFP is at present conventionally applied for domain engineering of LN, it suffers several drawbacks: i) the poor aspect ratio for fine domain period PPLN due to the sideways growth of the domains, ii) the difficulty of fabricating submicron-sized domains, iii) the high voltage required to pole thick crystals (because of the fixed value of E_c), and iv) the restrictions for writing arbitrary domain patterns due to the crystallographic preferences of the crystal (i. e., the domain walls preferentially align along the y-axes of the crystal).

There have been considerable research activities developing methods for domain reversal to overcome the draw-

[1] Optoelectronics Research Centre, University of Southampton, Highfield, Southampton, SO17 1BJ, UK [2] Centre for Photonics and Photonic Materials, Department of Physics, University of Bath, Bath, BA2 7AY, UK [3] currently at Cyrium Technologies Inc., Canada [4] Institute of Physics, University of Bonn, Wegelerstrasse 8, 53115 Bonn, Germany
[*] Corresponding author: e-mail: charlie0318@msn.com

Table 1 Forward coercive field (E_c) of some virgin crystals that were used in the experiment with various stoichiometry (Type) and Mg-dopings (Mg) (Mg doping level measured in the crystal instead of the melt is indicated by †) [31]. SZFKI = Research Institute for Solid State Physics and Optics.

Type	Mg [mol%]	E_c [kV mm^{-1}]	Supplier
CLN	0.0	21.9	Crystal Tech. (US)
CLN	2.5	12.7	SZFKI (HU)
CLN	3.5	10.2	SZFKI (HU)
CLN	4.5	7.5	SZFKI (HU)
CLN	5.0†	7.6	Yamaju Ceram. (JP)
CLN	5.5	6.0	SZFKI (HU)
CLN	6.5	6.7	SZFKI (HU)
CLN	7.5	7.4	SZFKI (HU)
SLN	1.0	2.4	Deltronic (US)

backs of EFP and thereby improving the quality and flexibility of domain formation. High temperature treatment has been used to reduce the value of E_c as reported in [12, 13] and possibly allowing for smoother domain growth. Other groups used electron [14] or ion [15] beam bombardment, or local application of the electric field using the tip of a scanning force microscope [16–18], or backswitched poling during EFP [19], to achieve the generation of submicron domains. To date, however, none of these attempts have lead to the highly desired breakthrough in the field of domain patterning.

A completely different method for domain engineering uses intense laser irradiation to either modify E_c or to directly induce ferroelectric domain inversion. This approach becomes particularly interesting as it overcomes issues such as the sensitivity to crystallographic directions and can also be applied in situations where EFP cannot be used (e. g., in the case of thin films or 'smart cut' sections deposited onto non-conductive substrates, or when the z-faces are not accessible for the application of the E-field). In this review, we present an overview of light-mediated methods for domain inversion in lithium niobate. We firstly list the optical properties of lithium niobate of different compositions relevant for our studies and present the experimental techniques used for generation and visualization of domains (Sect. 2). We then discuss separately the effect of ultraviolet-to-infrared light (Sect. 3) and of deep ultraviolet light (Sect. 4) on the domain formation. In Sect. 5 we demonstrate the fabrication of submicron scaled surface structures based on ferroelectric domain patterns.

2. Experimental basics

In this section we describe the experimental basics relevant for light-mediated domain formation in LN. At first we give information on the material itself, and give a list of the crystals and the laser light sources used (Sect. 2.1). Next we discuss methods to detect a domain pattern (Sect. 2.2) and finally give an overview of the techniques used to define the desired domain pattern (Sect. 2.3).

2.1. Properties of lithium niobate relevant for light-mediated domain engineering

The crystals used for most experiments are listed in Table 1. Generally, two types of lithium niobate crystals were utilized, of congruent and stoichiometric composition, abbreviated by CLN and SLN, respectively. Some of the crystals were doped with magnesium, which is the most prominent way to reduce optical damage [20], a restrictive factor for high intensity nonlinear optical applications. The optical damage threshold can be increased in doped crystals by ~ 2 orders of magnitude [21]. A clear indication that any dopant leads to increased resistance to optical damage is a shift of the OH-absorption peak from 2.87 to 2.83 µm (Fig. 1) occurring at Mg concentrations varying between 4.5 and 4.9 mol% for CLN [22, 23] and ~ 1 mol% for Mg:SLN [24–26] referred to as the optical damage threshold (ODT).

In the literature the nucleation field E_n is often used as an experimentally measured parameter instead of the coercive field E_c. The nucleation field is determined by the observation of micron-sized domain nuclei and is lower than E_c which corresponds to macroscopic domain inversion [27] or sometimes more specifically defined as the electric field for which the poling current exceeds a certain threshold of current (e. g., 1 µA [27, 28]). Normally the observed nuclei expand and develop into bulk domains with a further small increase of the field amplitude (or by prolonged application of the field) [29, 30].

For light-mediated domain inversion, the optical properties of lithium niobate of the different compositions used in the experiments are of major importance. Figure 1 shows the absorption spectrum of different crystals between 295 nm

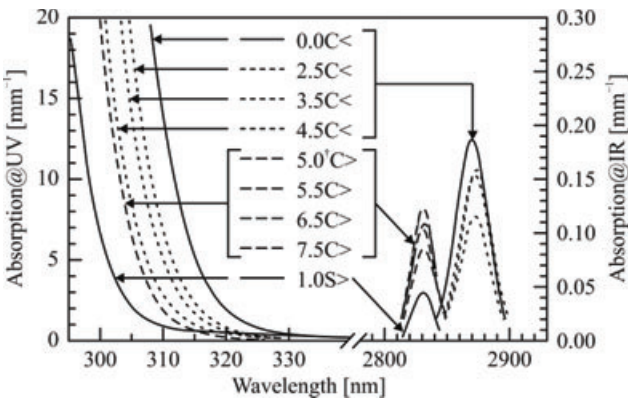

Figure 1 Absorption spectra for different crystals used in the experiments. The symbols for each line have the meaning of: number = Mg doping; 'C' or 'S' = congruent or stoichiometric LN; '>' or '<' = larger or smaller than the optical damage threshold. Mg doping level measured in the crystal instead of the melt is indicated by †. Replotted from [31].

and 3 µm. Roughly speaking, for wavelengths in the deep-UV range (< 300 nm) all crystals fully absorb the light near the surface, with a penetration depth on the order of 100 nm. Around the band-edge (300–320 nm) the absorption strongly depends on the exact crystal composition, and for the visible and the near-infrared spectral regions, the crystals are in general transparent. In the long-wavelength infrared, all LN crystals become absorbing again, with a penetration depth near 100 µm at a wavelength of 10.6 µm [32].

For all the light-mediated domain engineering experiments, a set of different lasers and wavelengths was used: continuous wave laser sources between 244 and 647 nm, pulsed lasers operating between 248 and 800 nm with pulse durations from 120–150 fs to 25 ns, and an additional CO_2 laser operating at 10.6 µm.

2.2. Visualization of domain patterns

For the visualization of the domain patterns three different techniques are commonly used:

1. After domain inversion, brief etching in hydrofluoric acid (48%) for several minutes. The $+z$ face resists etching while the $-z$ face is etched [34] and the obtained topographical patterns can be subsequently imaged by scanning electron microscopy (SEM) or using optical microscopy. The technique of domain-selective etching is very fast and allows imaging of large areas, but unfortunately destroys the surface of the crystal.
2. After domain inversion, using piezoresponse force microscopy (PFM) [35]. PFM is advantageous because it is non-destructive, however, it is very time consuming (imaging of $100 \times 100\,\mu m^2$ takes roughly one hour). The lateral resolution of PFM is of the order of 10 nm and the sensitivity depth is about 2 µm [36].
3. During domain inversion, whereby the crystal is mounted in a liquid-electrode holder and the refractive index distribution is detected. An index contrast can originate from i) the strain-induced birefringence at the domain wall [37, 38], ii) the refractive index change of newly poled domains in CLN [39], and iii) electro-optically induced refractive index differences between opposite domains [40]. A typical setup using a Mach-Zehnder interferometer for the visualization is shown in Fig. 2. A reference beam is used to interfere with the beam passing through the crystal. With an applied E-field, poled domains induce opposite phase shifts compared with the virgin domain via the electro-optic effect; therefore the setup is also known as *electro-optic visualization*. Via this phase-sensitive setup, even a phase difference given by a surface domain from the domain nucleation can be detected [41]. The ability for optical addressing of the crystal as well as the monitoring of the ferroelectric domain inversion process thus allows further control of the poling process.

2.3. Definition of the desired domain patterns

For application purposes it is essential to be able to fabricate specific and intentioned ferroelectric domain patterns. Patterning of domain structures has been achieved by i) direct writing, ii) two-beam interference, iii) using a phase mask or iv) an amplitude mask. We will briefly discuss advantages and disadvantages in the following.

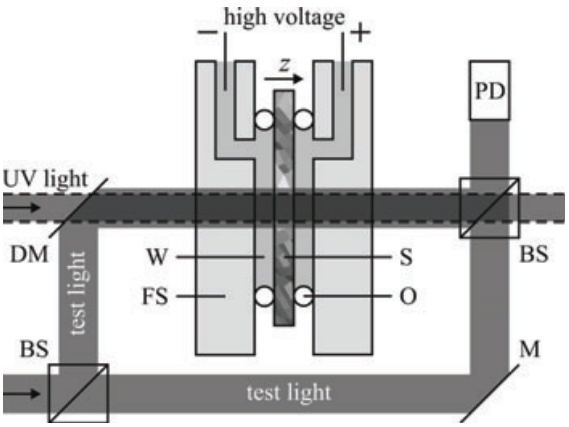

Figure 2 Setup for imaging the refractive index distribution. The sample, held between two transparent fused silica plates, is in contact with liquid transparent electrode. The light for light-assisted poling is indicated by the dashed lines. Test light is used for the visualization of the inverted domains as indicated in the schematic. W = water; S = LN sample; FS = fused silica; O = O-ring; BS = beam splitter; DM = dielectric mirror; M = normal mirror; PD = photodiode. Replotted from [33].

Direct writing

For direct writing a laser beam is scanned across the sample surface with the help of a computer-controlled translation stage. The first realization of this technique was performed by Dierolf et al. [42] where a 488 nm laser beam was focused 130 µm underneath the sample surface while applying an E-field to the crystal (Fig. 3a,b). The outstanding advantage of direct writing relies on its ability to write domain patterns free of the crystalline constraints, as best seen in Fig. 3c,d.

Two-beam interference

This is the technique of choice for obtaining a regular periodic pattern without the need of an expensive and time consuming photoresist mask. The laser beam is split into two beams which interfere at the sample surface. This is a suitable method for fabricating PPLN where many thousands of precisely defined periodically domain-inverted regions are required. The two beams for interference can either be incident on a face perpendicular to the z-face [44] or towards the z-face directly [27]. With the latter setup a quasi-periodic domain patten in Mg:CLN with period length of 55 µm and duty cycle of 0.63 has been realized (Fig. 4a). Note that along the y-axis of the crystal the desired stripes did not yet merge properly.

Phase mask

Apart from two-beam interference, another suitable domain patterning method for fabrication of PPLN uses a phase mask. This can eliminate the problem of vibrations and can

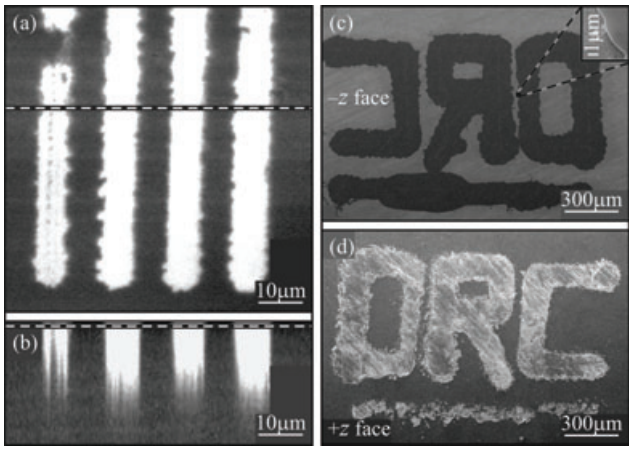

Figure 3 Direct writing. (a) Horizontal and (b) cross-section image of a domain structure in an Er-doped CLN sample. The dashed lines indicate the positions where the cross section was taken. Images were recorded with confocal luminescence microscopy. Replotted from [42]. (c) Front and (d) rear faces of a 500 μm thick CLN crystal with the ORC-logo inscribed using light-assisted poling technique (Sect. 3). Image was recorded by SEM after brief HF-etching. Replotted from [43].

therefore be used for longer exposures without loss of the fringe definition. Valdivia et al. [43] have realized such a setup and produced an intensity grating with 5.25 μm period using light of wavelength 514 nm. Clear definition of periodic domains was observed throughout the entire beam width in Mg:CLN as illustrated in Fig. 4c. To cover larger areas, the beam was scanned across the static phase mask. In this case, the irradiated area can be increased without

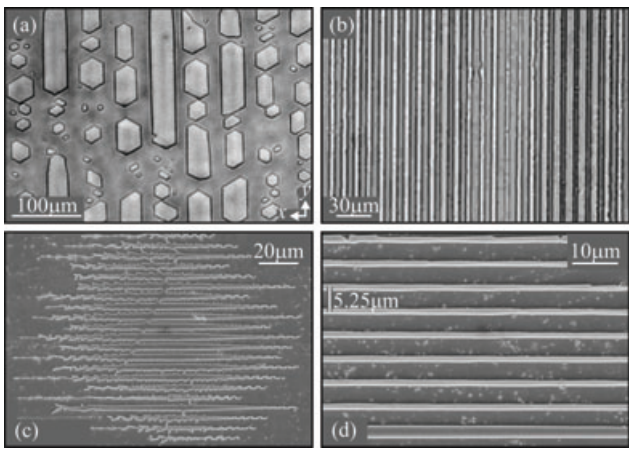

Figure 4 Domain patterns obtained in Mg:CLN (a,c,d) and Mg:SLN (b) crystals. (a) Two-beam interference. Microscopic image of the $+z$ face of a PPLN structure after wet etching in HF acid. Replotted from [27]. (b) Absorbing amplitude mask. Light microscopy image of HF-etched domain pattern. Replotted from [28]. (c) Phase mask using a light wavelength of 514 nm and illumination period of 5.25 μm. (d) Scanning the laser beam across the same static phase mask as in (c). Imaging of the generated domain patterns was performed by SEM after HF etching. Replotted from [43].

the loss of intensity. An example of a domain pattern obtained by using this method is illustrated in Fig. 4d with an achieved duty cycle of $\sim 25/75$.

Amplitude mask

Another method of domain patterning is the use of an amplitude mask directly deposited onto the sample surface. This can be for instance a structured Cr metal layer [45] or a structured photoresist [28], thereby reflecting and/or absorbing the light. Steigerwald et al. have used the latter scheme to generate a PPLN structure in Mg:SLN (Fig. 4b). More examples using contact mask or projected mask have been exploited by Valdivia [46].

3. Light-assisted poling

In this section, we will discuss the effect of a reduction of the coercive field E_c by irradiation of the crystal with weakly absorbed laser light (mainly visible to near-IR range but also some UV lines). This effect was first observed in Mg:CLN by Fujimura et al. [45]. For poling, in addition to the irradiation, an external, homogeneous E-field is applied to the crystal. This can be either in conjunction with the irradiation, referred to as 'light-assisted poling' (LAP) or subsequent to the irradiation, referred to as 'latent LAP' (Sect. 3.3). In terms of domain patterning, selective irradiation of the crystal leads to a spatially modulated E_c and hence results in spatially selective domain inversion in a homogeneous electric field, thereby eliminating the need for structured electrodes which are used in conventional EFP. Selective irradiation is performed using one of the schemes described above. In the last paragraph (Sect. 3.4) we will discuss the physics contributing to LAP.

The basic requirement for a LAP setup should allow the LN crystals to be addressed both optically and electrically. This can be achieved by irradiating along a direction normal to the E-field as in [44] which allows the use of opaque metal electrodes for the application of the E-field. A much more versatile setup for LAP is illustrated in Fig. 5. Here the crystal is mounted in a transparent fused silica holder using liquid-electrodes to apply the E-field (usually an aqueous solution of a salt or alternatively tap water works very well). The direction of irradiation of the crystal is therefore not restricted and can also take place along the direction of the E-field.

A general observation in LAP was that higher intensities of the irradiating laser beam result in a more pronounced reduction of E_c and E_n. However, the value of this reduction depends also on the specific crystal type (stoichiometry, dopant and doping level) as well as the wavelength of the laser utilized. The highest reduction of E_n ($> 98\%$) has been observed in 5 mol% Mg:CLN [43, 46] and in 1 mol% Mg:SLN [50] using a pulsed and a c. w. laser source, respectively, at visible wavelengths. In both cases the MgO doping level was above the ODT. The maximum E_n reduction which has been observed in undoped CLN was of the order of 40% using irradiation with a fs-pulsed

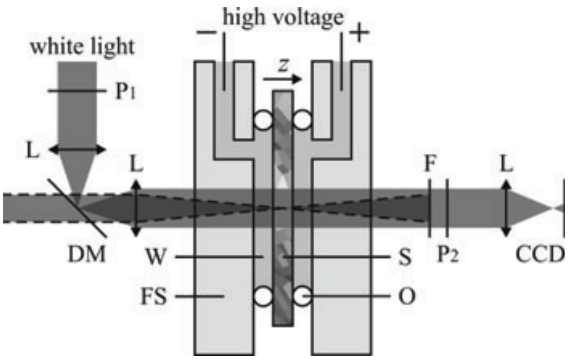

Figure 5 Schematics showing the standard LAP setup, thereby allowing for simultaneously irradiating the crystal while applying an electric field to it using liquid electrodes. The light for light-assisted poling is indicated by the dashed lines. The white light is used for the simultaneous visualization of the poling process. P_1, P_2 = crossed polarizers; L = lens; F = filter to block the irradiating light for LAP; DM = dielectric mirror; W = water; S = LN sample; FS = fused silica; O = O-ring; CCD = CCD camera. Replotted from [29].

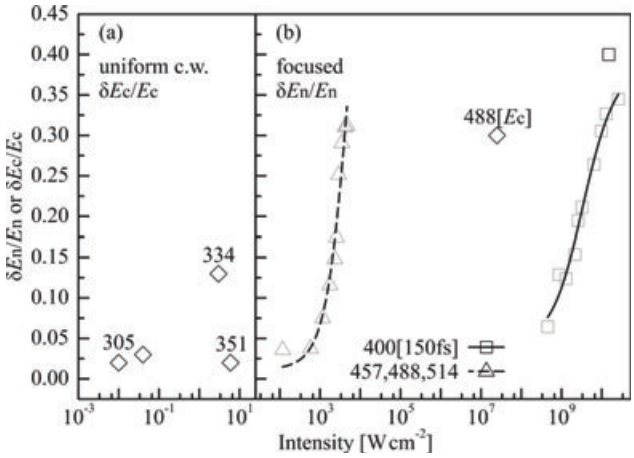

Figure 6 Relative reductions of the nucleation field E_n or the coercive field E_c as a function of intensity (or peak intensity for pulsed laser irradiation) achieved by LAP in undoped CLN obtained from literature. All the grey dots have been guided with curves as guides for the eye. The individual black □ on the top right was obtained from an experiment separate from those grey ones guided with the curve. (a) E_c reduction achieved in c. w. LAP with uniform illumination. (b) E_n reduction (unless marked as [E_c] for E_c reduction) achieved in LAP with focused laser light irradiation. The numbers next to the black symbols correspond to the illuminating wavelength in unit 'nm'. All the lasers used in (a) and (b) are c. w. lasers, apart from the 400 nm fs-laser (150 fs) marked by symbol □.

laser beam at 400 nm [43, 46]. Due to the significant difference between undoped and Mg-doped LN in terms of defect structure, photoconductivity and UV absorption edge, we will treat the two crystal types separately in the following paragraphs.

3.1. LAP with undoped congruent LN (CLN)

LAP has been observed in CLN using either c. w. laser sources with wavelengths ranging from 305 to 514 nm or pulsed laser sources at 400 nm, mostly within the transparency window of the crystal which is ∼ 350 nm to 5 µm [51]. An E_n reduction was observed with increasing laser intensity which reaches 32% in the c. w. case and 40% in the pulsed case. Domain nucleation has generally been observed on the $-z$ face of the crystal irrespective of the illuminated face except at 305 nm where nucleation occurred on the face opposite to the irradiated one [27]. In some cases, the reduction of E_n can be preserved during a subsequent dark forward poling process [27, 33, 49]. A summary of the exposure conditions and corresponding results is presented in Table 2. Results from the literature on the reductions of E_n or E_c as a function of the irradiating laser intensity are shown in Fig. 6.

3.2. LAP with magnesium doped LN (Mg:CLN and Mg:SLN)

LAP in magnesium-doped crystals was first demonstrated by Fujimura et al. [45]. Subsequent detailed investigations

λ [nm]	C/P	IF	FC	IT [W cm^{-2}]	NF	E_c(min)/E_c(dark) [kV mm^{-1}]	RD [%]	P	Ref.
305	c. w.	$-z$	plane	10^{-2}		21.09/21.59	2		[47]
305	c. w.	$\pm z$	plane	4×10^{-2}	$\mp z$	20.55/21.19	3	Y	[27, 48]
334	c. w.	$-z$	plane	3		17.1/19.75	13	Y	[33]
351	c. w.	$-z$	plane	6		19.5/19.9	2	N	\/
400	150	$-z$		1.5×10^{10}	$-z$	12.5/20.81 (E_n)	40		[43, 46]
457, 488, 514	c. w.	$\pm z$	$-z$	3×10^{3}	$-z$	14.3/20.9 (E_n)	32		[29]
488	c. w.	$\pm z$	in bulk	2.5×10^{7}	$-z$	15.4/22	30		[42]
514	c. w.	z			$-z$	20/22.57	11	Y	[49]

Table 2 LAP for undoped CLN. λ = wavelength; C/P = c. w./pulsed laser; IF = incident face of light; FC = focussing conditions; IT = intensity or peak intensity for pulsed laser; NF = nucleation face; $E_c(\min)$, $E_c(\text{dark})$ = minimum achieved via LAP, and dark forward coercive field; (E_n) = nucleation field was investigated instead of coercive field; RD = reduction in %; P = whether the reduction was preserved during the subsequent forward poling in dark; \/ = same reference as the row above.

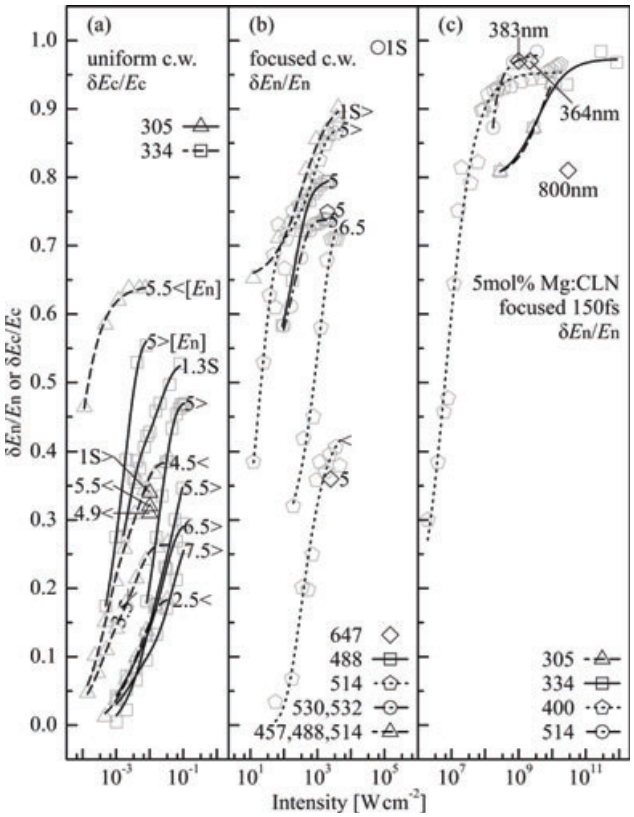

Figure 7 Relative reductions of nucleation field E_n or coercive field E_c as a function of intensity (or peak intensity for pulsed laser irradiation) achieved by LAP in Mg:LN obtained from literature. All the grey dots have been guided with curves as guides for the eye. (a) E_c reductions (unless marked as $[E_n]$ for E_n reduction) achieved in c. w. LAP with uniform illumination. (b) E_n reduction achieved in c. w. LAP with focused laser light irradiation. In (a) and (b) the marks next to the curves or black symbols correspond to: number = mol% Mg doping; 'S' = stoichiometric LN (if not marked 'S' then the material is congruent); '>' or '<' = doping larger or smaller than the optical damage threshold. (c) E_n reductions of 5 mol% Mg:CLN achieved in LAP using focused fs-laser light (150 fs). The numbers for dots correspond to the irradiating wavelength.

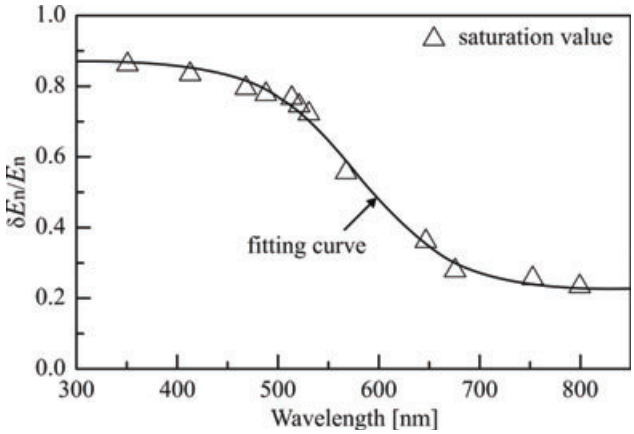

Figure 8 Plot showing the saturated factional reduction of nucleation field ($\delta E_n/E_n$) in forward LAP of 5 mol% Mg:CLN for incident wavelength from 351 to 799 nm. Replotted from [54].

of LAP in Mg:LN of different doping level and stoichiometry have been conducted by various groups using c. w. and pulsed laser sources with wavelengths ranging from 305 to 800 nm. All the LAP results from literature for Mg:LN have been summarized in Table 3 and Fig. 7. In the following we describe the experimental results in detail which can be subdivided in LAP obtained by continuous wave (c. w.) and by pulsed laser irradiation.

Continuous wave laser irradiation

Continuous wave laser LAP showed reductions of E_n by 88% for Mg:CLN at wavelengths of 457, 488, and 514 nm with intensity $I = 3 \times 10^3\,\mathrm{W\,cm^{-2}}$ [29] and 99% for Mg:SLN at 532 nm with $I = 6.4 \times 10^4\,\mathrm{W\,cm^{-2}}$ [50]. As for the saturated reduction values the experimental results are not conclusive: Sones et al. observed no wavelength dependence but found similar reduction of E_n for 457, 488 and 514 nm [29] whereas Zhi et al. reported a wavelength dependence: a higher saturated reduction for shorter wavelength [54] as shown in Fig. 8. The nucleation field reduction of Mg:CLN irradiated with 488 nm was observed to be preserved during the subsequent forward poling in dark [54], while Wengler et al. have reported the preservation of reduction at 305 nm LAP of MgO doping below the ODT [27]. However, Wang et al. provided some clues that the post effects of LAP light irradiation during the subsequent EFP might be erased by uniform UV illumination [49]. As indicated in Table 3, nucleation occurs in most cases on the $-z$ face, apart from when using 305 nm in Mg:CLN [27], 334 nm in Mg:SLN [28] and heat-involved LAP in Mg:CLN [13].

Studies of the impact of MgO doping revealed that crystals with MgO doping lower than the ODT showed no [27, 47, 48] or much less [46] reduction of E_c or E_n compared with crystals with higher than ODT MgO levels for the same irradiation conditions. In the case of 305 nm illumination, however, the effect was reversed with the observation of latent effects for doping levels below the ODT while at doping levels above the ODT severe optical damage was observed even at intensities as low as $10^{-2}\,\mathrm{W\,cm^{-2}}$.

The stability of LAP nucleated domains in Mg:LN has been investigated by i) multiple post poling cycles showing that LAP domains do not invert back at E_c field amplitudes and ii) by heating the samples to temperatures up to 600 °C [49].

Pulsed laser irradiation

Pulsed laser LAP has been successfully demonstrated using laser sources with a pulse width of 120–150 fs and wavelengths between 305 and 800 nm. An E_n reduction higher than 90% has been obtained in Mg:CLN and Mg:SLN crystals doped higher than ODT [43, 46]. Even for irradiation at much longer wavelength (800 nm) significant E_n reduction ($> 80\%$) has been observed in Mg:CLN.

Table 3 LAP for Mg:LN. Type = stoichiometry; Mg = mol% Mg doping (Mg doping level measured in the crystal instead of the melt is indicated by †); ODT = doping is higher than the optical damage threshold; λ = wavelength; C/P = c. w./pulsed laser; IF = incident face of light; FC = focussing conditions; IT = intensity or peak intensity for pulsed laser; NF = nucleation face; $E_c(\mathrm{min}), E_c(\mathrm{dark})$ = minimum achieved via LAP, and dark forward coercive field; (E_n) = nucleation field was investigated instead of coercive field; RD = reduction in %; P = the persistence of reduction in the subsequent forward poling in the absence of light; ∨ = same reference as the row above.

Type	Mg [mol%]	ODT	λ [nm]	C/P [fs]	IF	FC	IT [W cm^{-2}]	NF	$E_c(\mathrm{min})/E_c(\mathrm{dark})$ [kV mm^{-1}]	RD [%]	P	Ref.
LN	5		UV	c. w.	$\pm z$	plane	2×10^{-1}	$-z$	3.5/–			[45]
SLN	1	Y	334	c. w.	$-z$	plane	10^{-2}		2.49/2.49	0		[47]
CLN	4.9	N	334	c. w.	$-z$	plane	10^{-2}		5.94/5.94	0		∨
CLN	5.5	N	334	c. w.	$-z$	plane	10^{-2}		6.31/6.31	0		∨
CLN	5†	Y	334	c. w.	$-z$	plane	10^{-2}		4.99/6.8	27		∨
SLN	1	Y	305	c. w.	$-z$	plane	10^{-2}		1.64/2.49	34		∨
CLN	4.9	N	305	c. w.	$-z$	plane	10^{-2}		4.08/5.94	31		∨
CLN	5†	Y	305	c. w.	$-z$	plane	10^{-2}		damage			∨
CLN	5.5	N	305	c. w.	$-z$	plane	10^{-2}		4.28/6.31	32		∨
CLN	5†	Y	457–514	c. w.	$+z$	$-z$	3×10^{3}	$-z$	0.78/6.28 (E_n)	88		[29]
SLN	1	Y	457–514	c. w.	$+z$	$-z$	3×10^{3}	$-z$	0.28/2.63 (E_n)	89		∨
CLN	7.5	Y	334	c. w.	$\pm z$	plane	10^{-1}	$-z$	5.23/7.04	26	N	[27,48]
CLN	6.5	Y	334	c. w.	$\pm z$	plane	10^{-1}	$-z$	4.54/6.4	29	N	∨
CLN	5.5	Y	334	c. w.	$\pm z$	plane	10^{-1}	$-z$	4.04/6.21	35	N	∨
CLN	5†	Y	334	c. w.	$\pm z$	plane	10^{-1}	$-z$	3.41/6.44	47	N	∨
CLN	5†	Y	334	c. w.	$\pm z$	plane	10^{-2}	$-z$	2.70/6.09 (E_n)	56	N	∨
CLN	5†	Y	305	c. w.		plane			damage			∨
CLN	5.5–7.5	Y	305	c. w.		plane			damage			∨
CLN	5.5	N	305	c. w.	$\pm z$	plane	10^{-2}	$\mp z$	2.09/5.80 (E_n)	64	Y	∨
CLN	4.5	N	305	c. w.	$\pm z$	plane	4×10^{-2}	$\mp z$	4.97/7.77	39	Y	∨
CLN	3.5	N	305	c. w.	$\pm z$	plane	4×10^{-2}	$\mp z$	7.84/10.74	27	Y	∨
CLN	2.5	N	305	c. w.	$\pm z$	plane	4×10^{-2}	$\mp z$	10.47/12.77	18	Y	∨
CLN	5		647	c. w.	$\pm z$	$\pm z$	2.5×10^{3}	$-z$	2.88/4.5 (E_n)	36		[52]
CLN	5		514	c. w.	$\pm z$	$\pm z$	2×10^{3}	$-z$	1.12/4.5 (E_n)	75		∨
SLN	1		400	150	$-z$		1.2×10^{10}	$-z$	0.17/2.65 (E_n)	94		[43,46]
CLN	5	Y	305	150	$-z$		10^{10}	$-z$	0.4/6.337 (E_n)	94		∨
CLN	5	Y	334	150	$-z$		3×10^{11}	$-z$	0.1/6.337 (E_n)	98		∨
CLN	5	Y	364	150	$-z$		2.2×10^{9}	$-z$	0.2/6.337 (E_n)	97		∨
CLN	5	Y	383	150	$-z$		10^{9}	$-z$	0.2/6.337 (E_n)	97		∨
CLN	5	Y	400	150	$-z$		1.8×10^{10}	$-z$	0.22/6.337 (E_n)	97		∨
CLN	5	Y	514	150	$-z$		3.6×10^{9}	$-z$	0.1/6.337 (E_n)	98		∨
CLN	5	Y	800	150	$-z$		3×10^{10}	$-z$	1.2/6.337 (E_n)	81		∨
SLN	1		514	c. w.	$\pm z$		4×10^{3}		0.8/2.35	66		[53]
CLN	5		488	c. w.	$\pm z$	$\pm z$	2×10^{3}	$-z$	0.945/4.5 (E_n)	79	Y	[54]
CLN	5		530	c. w.	$\pm z$	$\pm z$	2×10^{3}	$-z$	1.17/4.5 (E_n)	74		∨
LN	5		514	c. w.	z			$-z$	5.09/8.29	39		[49]
LN	6.5		514	c. w.	z		3×10^{3}	$-z$	1.42/4.90	71		∨
SLN	1.3		334	c. w.	$\pm z$	plane	8×10^{-2}	$+z$		53		[28]
CLN	5		351	c. w.	$\pm z$	plane	10^{-2}	$+z$				[13]
SLN	1		532	c. w.		$-z$	6.4×10^{4}	$-z$	0.03/2.4 (E_n)	99		[50]

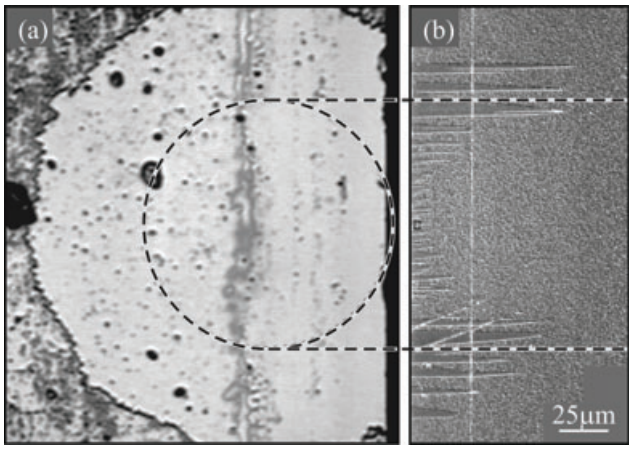

Figure 9 Circular LAP domain in Mg:CLN exposed to 1.2 GW cm^{-2} peak intensity, 400 nm wavelength with a simultaneously applied E-field of 1 kV mm^{-1}. The exposure time is 2 sec. (a) Optical microscope image of the etched $-z$ face. (b) SEM micrograph of the etched y-face profile below the $-z$ face. The dashed lines enclose the area of irradiation. Replotted from [46].

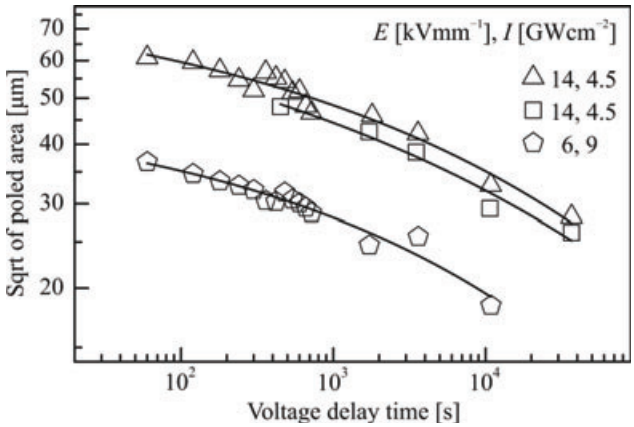

Figure 10 Plot of the square root of the inverted latent-LAP domain area, as a function of the voltage application delay time for different E-field amplitudes and laser intensities I as indicated in the legend in units kV mm^{-1} and GW cm^{-2} respectively. The irradiating source is a 400 nm fs-laser with $\sim$ 30 μm beam diameter. The solid lines serve as a guide to the eye. Replotted from [56].

Studies of the depth profile of LAP domains have been conducted using HF etching of a polished y-face cross section. Figure 9 shows optical microscope images of a LAP domain obtained in Mg:CLN. The cross section in Fig. 9b reveals that the depth profile is not uniform but is a function of the distance from the centre of the circle with the central part being shallower than the periphery. The dashed circle and pair of dashed lines in a and b respectively enclose the irradiated area which overlaps with the boundary between the shallow and deep domain areas. The domain depth profile also appears to be consisting of spikes which are typically observed in the propagation of domains between opposite polar faces. Additionally, the deeper domains in the periphery can be influenced by the laser irradiation, more specifically, increase with longer irradiation times while the central domains maintain a depth of $\sim$ 15 μm regardless the exposure time. The difficulty of pushing the central domain deeper into the bulk region by post application of a uniform E-field is in line with the further observation that, during post bulk poling of the whole crystal at a higher poling field, the shallow central domain can even inhibit the local bulk poling as reported in [55].

3.3. Latent light-assisted poling (latent LAP)

In all cases of LAP reported thus far, the application of the external E-field was simultaneous with the irradiation. However, Ying et al. reported that in CLN a reduction of E_n can be observed for even several hours after irradiation with short (120–150 fs) laser pulses at a wavelength of 400 nm [56]. This latent LAP allows for de-coupling of the two processes of light illumination and application of an external E-field. Additionally, the E_n reduction which was observed in latent LAP is 62% which was higher than the corresponding reduction observed in normal LAP (40%) using the same irradiation conditions [43]. The square root of the domain inverted area as a function of the time delay between light illumination and application of the external E-field is shown in the plot of Fig. 10. Latent-LAP, though attempted, has not been observed in Mg:CLN for the observation time scales employed in the experiments.

The observation of latent-LAP in undoped CLN, and the dependence of the domain inverted area on the delay time between irradiation and E-field application suggest that the effect is caused by the formation of a photo-induced space charge distribution which decays with time in the absence of light. The presence of a photo-induced space charge distribution has been verified by photorefractive experiments using the same laser source. The relaxation dynamics of photorefractive gratings recorded in undoped CLN crystals were observed to be very similar to the size dependence of latent-LAP domains with voltage application delay times. Furthermore, photorefractive experiments in Mg-doped crystals have shown that i) the photorefractive grating diffraction efficiency was significantly higher as compared to the undoped CLN and ii) the grating dark decay was much faster than the voltage delay times used in the latent-LAP experiments [56]. These observations provide justification for the large E_n reductions which were observed in LAP experiments for Mg:CLN [43] and also for the absence of latent-LAP in Mg:CLN.

3.4. Discussion of possible LAP mechanisms

Several physical mechanisms have been suggested to explain the LAP process. These include the *formation of a photo-induced space charge field* which assists the effect of the externally applied poling field, the *screening of surface defects* which are responsible for pinning of the domain wall, and finally the *formation of new photo-induced defects*. As LAP has been observed in a variety of different

LN crystals (in terms of stoichiometry and doping) and using different spectral ranges, these mechanisms can have a material/wavelength dependent validity.

3.4.1. Photo-induced space charge field

A photo-induced space charge field along the direction of the externally applied electric field can be formed by i) direct photo-excitation of electrons from impurity defects followed by their diffusion [42, 49], ii) photoconductivity gradient induced electric field (especially for high absorbing c. w. 305 nm illumination [27]), and/or iii) the photovoltaic effect [41, 57].

In the case of visible light illumination, electrons can be excited from Fe^{2+} defect levels to the conduction band, then after diffusion get re-trapped in Fe^{3+} impurity levels and leave behind uncompensated positive charges, thus forming a space charge distribution which in turn produces a space charge field. As proposed in [49] and [42], the schematics shown in Fig. 11a and b illustrate the process of photo-ionization and diffusion for uniform and focused laser irradiation respectively, which in both cases form a space charge field $\mathbf{E}_{sc}$ parallel the poling field at the $-z$ face. This explains the very common observation that preferential domain nucleation happens primarily on the $-z$ face.

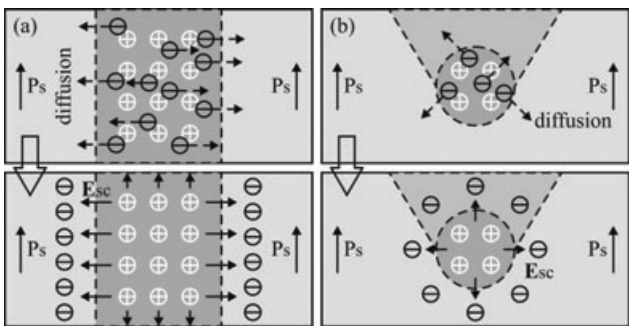

Figure 11 Schematic illustrations of space charge field produced upon photo-excitation of electrons and their subsequent diffusion (a) for uniform illumination and (b) for focused irradiation. The dash line enclosed regions correspond to the irradiated regions. P_s = spontaneous polarization; $\mathbf{E}_{sc}$ = space charge field. (a) is replotted from [49].

Exceptions from the situation discussed above are observed for shorter wavelengths, below the absorption edge of the crystal. In the case of c. w. 305 nm laser illumination LAP can only be observed for an MgO doping level lower than the ODT, while domain nucleation was observed to occur primarily on the face which is opposite the illuminated one [27]. Wengler et al. [27] have calculated an inhomogeneous E-field distribution through the crystal thickness which is produced by the gradient in electrical conductivity as a consequence of the significant absorption at the irradiating wavelength over the thickness of the sample. The calculated E-field appears to have a maximum at the opposite face as shown in the graph of Fig. 12 which explains

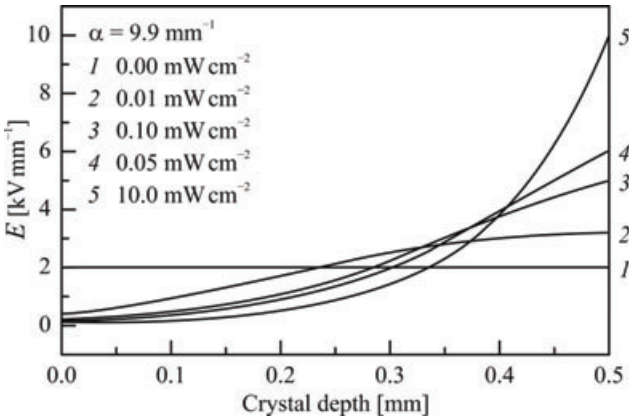

Figure 12 Modeled E-field distribution versus crystal depth with light incident on the crystal face. The thickness of the crystal is 0.5 mm. The absorption coefficient is 9.9 mm^{-1}. The five different curves correspond to five different intensity levels. Replotted from [27].

the face selective nucleation of domains observed in those experiments.

The role of the photovoltaic effect in LAP has also been considered by [41, 57]. During laser illumination, a photovoltaic current is produced described by $\mathbf{j}_{pv} = \alpha k_G I \hat{\mathbf{z}}$, where α is the absorption coefficient; k_G is the Glass constant; I is the incident intensity; and $\hat{\mathbf{z}}$ is the unit vector along the $+z$ axis. The photovoltaic current points towards the $+z$ axis: electrons drift towards the $-z$ face. The accumulation of electrons on the $-z$ face and the remaining uncompensated positive charges form a space charge field $\mathbf{E}_{sc}$ along the $-z$ axis and assists the externally applied poling field. The process is illustrated schematically in Fig. 13.

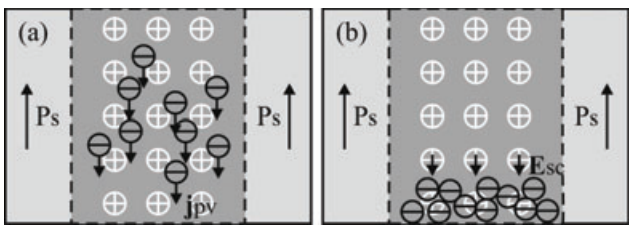

Figure 13 Schematic showing the formation of space charge field $\mathbf{E}_{sc}$ via photovoltaic effect. (a) Electrons drift towards the $-z$ face due to the photovoltaic effect during light illumination (dashed line enclosed region). (b) The accumulated electrons on the $-z$ face and the uncompensated positive charges form a space charge field $\mathbf{E}_{sc}$ parallel the $-z$ direction. P_s = spontaneous polarization; $\mathbf{E}_{sc}$ = space charge field.

3.4.2. Screening of surface defects

Photo-excited charges on the surface can also screen surface defects which are responsible for the pinning of domain walls [58]. The attribution of the observed photo-induced E_n reduction to the screening of defect centers was first proposed by [27, 29] and is supported by the observation

that domain growth at low E-fields is dominated by domain pinning [59]. The amount of domain pinning is strongly dependent upon the stoichiometry of the crystal and increases with the defect density.

The way that photo-excited charges screen the defect cluster in CLN might be straightforwardly attributed to the presence of Nb_{Li}^{4+} polarons and/or V_{Li}^{+} polarons. The spontaneous polarization in CLN is actually stabilized by the defect cluster composed of one Nb_{Li}^{5+} and four V_{Li} [59]. Thus, electrons on Nb_{Li}^{5+} (Nb_{Li}^{4+} polarons) and holes on V_{Li} (V_{Li}^{+} polarons) can screen the defect cluster. This screening can greatly reduce the contribution of the defect clusters to the stabilization of the spontaneous polarization (thus reducing the effective E_c).

For Mg:LN, the defect center responsible for light-induced reduction of pinning must be related to the MgO doping. This is because much higher E_c reduction has been observed at doping levels >ODT during c. w. 334 nm LAP [27]. Considering that at the ODT, all Nb_{Li} antisite defects are completely substituted by Mg_{Li} defects [60], it suggests that for Mg:LN the Mg_{Li} might be the responsible pinning defect that is to be screened by the photo-excited charges.

3.4.3. Photo-induced defects

It was proposed by Müller et al. [33] that intense UV radiation can produce additional defects in crystals. These defects provide nucleation sites during the early stages of the poling process and, therefore, enable the domain wall movement to start at lower E-fields. Zhi et al. [54] further expands the explanation that the additional defect structures are generated by the complex co-operative interaction of an incident irradiation field and an external E-field. These defect structures act as the nucleation centers. Experimental support has been provided by the indication of crystal lattice deformation at the center of a c. w. 488 nm LAP domain, observed via digital holographic interferometry. Figure 14a shows the interferogram of the LAP domain while b shows the phase shift profiles along the three directions indicated in a. The size of deformation matches that of the focal spot, and it was observed to trigger preferential domain nucleation in subsequent poling cycles in the absence of laser irradiation. This deformation is thought to be a large cluster of defects induced by the intense laser irradiation acting as a nucleation center during EFP.

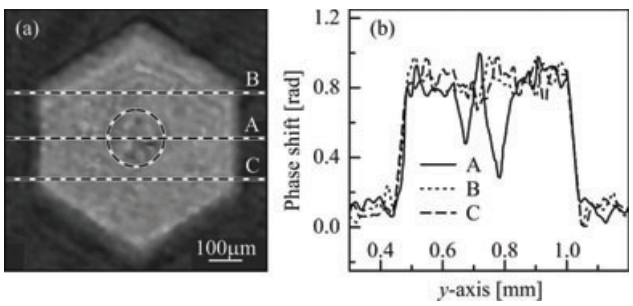

Figure 14 (a) Holographic interferogram of a c. w. 488 nm LAP domain in 5 mol% Mg:CLN which shows a deformation overlapping with the laser irradiated area (dashed circle). (b) Three scanning lines A, B, and C in (a) selected for showing the phase information of transverse section across the LAP domain. Replotted from [54].

3.4.4. Other mechanisms

Laser-induced heating of the crystal in the visible spectral region has been excluded by several authors. Dierolf et al. [42] performed micro-Raman measurements using a confocal microscope and observed the intensity ratio of the Stokes/anti-Stokes response of several vibrational modes showing that the temperature increase is less than 10 K for c. w. 488 nm illumination at intensities of order 10^8 W cm^{-2}. However, a thermally induced E_c reduction of 75% corresponds to a crystal temperature of 250 °C (for Mg-doped LN), which is too high for the laser intensities used in LAP experiments. The non-thermal origin of the coercive field reduction also accords with the observation that in some experiments the E_c or E_n reduction can persist for some time after the LAP experiment [27, 33, 49, 54], much longer than the equivalent cooling time.

Each of the mechanisms which have been outlined earlier can explain some of the effects that constitute LAP and latent-LAP. However, the variety of laser sources in terms of wavelength and peak intensity as well as the plethora of crystal stoichiometries and doping suggests that in many cases it is an interplay of several physical mechanisms which is responsible for the observed effects rather than a single one.

4. UV laser-induced poling

Laser irradiation of a crystal surface with deep-UV light induces completely different effects on the poling from those obtained by visible-IR illumination described in Sect. 3. This is mainly due to the strong absorption of deep-UV light that leads to high temperatures (together with steep temperature gradients) at the sample surface which can reach and even exceed the melting temperature. Deep-UV irradiation leads either to inhibition of poling during a subsequent electric field poling step (Sect. 4.1) or to directly poled surface domains referred to as all-optical poling (Sect. 4.2). We will finally discuss the origin of UV laser-induced poling (Sect. 4.3).

4.1. Poling inhibition (PI)

Poling inhibition (PI) denotes the phenomenon whereby a previously UV-irradiated area resists subsequent electric field poling (EFP): laser irradiation in this case is always performed with a c. w. laser. To state it precisely: PI is a two-step procedure comprising local UV-irradiation followed by homogeneous EFP. The physical origin of PI is basically an increase of E_c or E_n as a consequence of laser irradiation, as

Table 4 Results of poling inhibition from the literature. λ = wavelength of the c. w. laser; IF = incident face of light; IT = intensity; \" = same reference as the row above; $\times$ = several.

Crystal	λ [nm]	IF	IT [W cm^{-2}]	Depth [μm]	Ref
LT	488 & 514			bulk	[61]
LT	351 & 364	$+y$	10^2		[62]
CLT	351 & 364	y			[44]
CLN	275–305	$+z$	$\times 10^5$	1.5–4.3	[63]
CLN Mg:CLN	244	$+z$	$\times 10^5$		[64]
CLN SLN Mg:CLN Mg:SLN	275	$+z$	$\times 10^5$	$\times 1$	[65]

will be discussed in detail later. The PI results from literature have been summarized in Table 4.

Poling inhibition was first observed in lithium tantalate after irradiation at 488 and 514 nm [61]. With illumination of 351 and 364 nm laser light, modulation of the domain profile has been demonstrated via light propagating through a binary grating [62] which was further improved by direct illumination of a biprism-polished y-face to split the beam for two beam interference that produced a 6.3 μm domain period [44].

Poling inhibition in LN crystals was initially observed by UV-irradiating ($\lambda = 244$ nm) the $+z$ face of undoped and Mg-doped CLN crystals [64]. Later it was found that the effect could also be achieved using longer UV laser wavelengths of up to 305 nm [63]. Typical parameters of the irradiating laser beam used for PI are a spot diameter of 3–6 μm, and a laser power between 20–50 mW. In order to define a domain pattern, the laser beam is scanned across the surface with a typical writing speed between $v = 0.1$ and 1 mm s^{-1}. Good quality continuous PI domains could be obtained by maintaining slow domain wall velocities during the EFP step which can be achieved by using preferably low poling voltages. As for the crystals, PI was found to work best in CLN and Mg:CLN, and could partially be realized in stoichiometric compositions. The thermal stability of PI domains has been ascertained by heating the samples to temperatures up to 300 °C for 30 h without observing any deterioration of the domain structure. Note that PI in LN basically takes place only when irradiating the $+z$ face of the crystal.

Figure 15 shows a circular PI domain generated by a spot-irradiation ($\lambda = 244$ nm, beam diameter ≈ 5 μm) of the $+z$ face of a undoped CLN crystal. The SEM image a and the corresponding PFM image b both support the evidence that the laser-irradiated spot was not poled in the subsequent EFP step, as it still exhibits a $+z$ face, while the surrounding area corresponds to a $-z$ face. At the center of the PI domain, a surface damaged area of ~ 2 μm diameter can be seen,

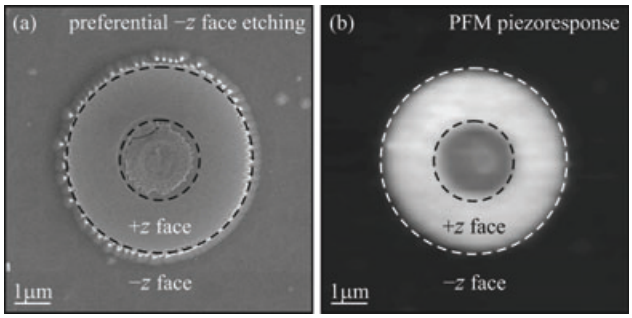

Figure 15 (a) SEM image of a briefly etched circular poling-inhibited domain ($+z$ face) in undoped CLN. (b) Corresponding PFM image of an identical domain before etching. The enclosed dashed circles are guides to the eye for comparing the domain shape to a perfect circle.

which, in the PFM image exhibits a slightly reduced contrast. This area can be associated with a shallow ($\sim$ nm deep) directly poled layer (to be discussed in Sect. 4.2.1).

The depth, the width, and the surface quality of poling-inhibited domains have been investigated as a function of UV writing conditions (Fig. 16). The achievable domain depths were found to range from 1.5 to 4.3 μm and the widths from 2.9 to 12.3 μm. The depth of the poling-inhibited domains was measured by wedge-polishing the sample perpendicular to linear PI domain tracks at a shallow angle ($\approx 5°$) as shown in Fig. 17. The depth profile of the domains can in this way be spread-out for better investigation.

Figure 16 also reveals that depth and width were largely insensitive to the UV laser wavelength used (from 275 to

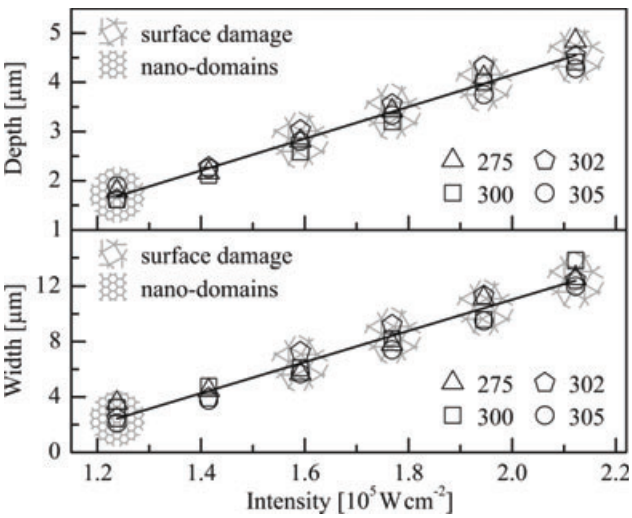

Figure 16 Depth (top) and width (bottom) of PI domains in undoped CLN as a function of the irradiating laser intensity for different UV laser sources with wavelengths: 275, 300, 302, and 305 nm. The writing speed is 1 mm s^{-1} and the beam diameter is ~ 6 μm. The lines represent linear fittings of the experimental data and the symbols correspond to the different surface qualities shown in Fig. 17. Replotted from [63].

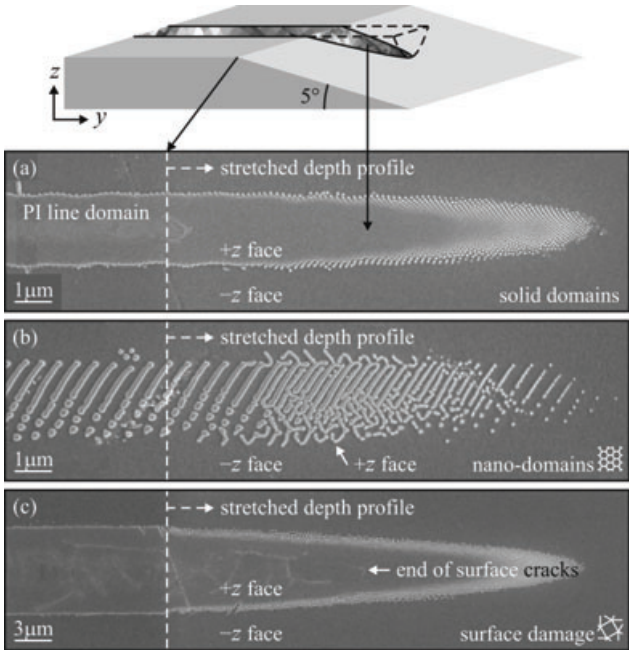

Figure 17 SEM images of the etched wedge-polished PI domains showing the stretched depth profile. The PI domains are fabricated under different conditions showing the three different quality categories: (a) solid good quality continuous PI domains of type i), (b) non-solid domains of type ii) consisting of single stripe-like nano-domains, and (c) solid continuous domains but with laser-induced surface damage (type iii). The circular nanodomains best seen in (a) indicate that the boundary of the domain is rough. The dashed line indicates the start of the wedge.

305 nm) for identical writing conditions (intensity, exposure time, spot size). The quality of the resulting PI domains can be categorized as follows: i) solid good quality continuous domains, ii) non-solid domains consisting of a (often dense) distribution of nano-domains, and iii) solid continuous domains but with laser-induced surface damage. These three different domain types are illustrated in SEM images of the wedge-polished domains in Fig. 17. As can be seen from Fig. 16, the highest quality domains are obtained for a laser intensity of $1.4 \times 10^5\,\mathrm{W\,cm^{-2}}$ whereas lower intensity results in domains of type ii) and higher intensity leads to type iii) domains.

The formation of PI domains was found to be insensitive to overwriting, i. e., a domain crossing can be readily generated by subsequently writing two laser tracks. Figure 18a shows an example, which is even more interesting as it underlines once more that light-mediated domains are not influenced by the crystallographic constraints of the threefold rotation symmetry in LN. Note that from the domain pattern itself it is not possible to tell which of the two tracks has been written first. As for the minimum distance between two domains Fig. 18b shows an impressive example where two parallel PI-domains are separated by a submicron gap only. All these characteristics provide a flexible and reliable tool for domain engineering and as we will see later for micro-structuring of LN crystals (Sect. 5).

4.2. All-optical poling (AOP)

Irradiation of LN crystals with intense UV radiation can, under certain conditions, lead to local domain inversion without the application of any external electric field or in other words induce all-optical poling (AOP). AOP has been observed in undoped and Mg/Fe/Ti-doped CLN using a variety of UV laser sources (c. w. and pulsed) in the UV (244–308 nm) and infrared (10.6 μm) spectral range at intensities which approach the damage threshold of the surface. The depth of the resulting AOP domains is a few microns and their width can be as small as ≈ 150 nm. The method of AOP could therefore provide an alternative approach for domain engineering of thin films of lithium niobate or 'smart cut' sections deposited onto insulating substrates which in general pose an obstacle to electric field poling. In the following the cases of c. w. and pulsed laser irradiation will be investigated separately due to the enormous differences in the irradiation time scales and intensities which generally yield qualitatively different results. The results of all-optical poling from the literature have been summarized in Table 5.

4.2.1. AOP using c. w. laser irradiation

In this section we present results obtained by scanning a c. w. laser beam across the sample surface. All domain patterns were therefore obtained by sequential direct writing with a laser beam.

Irradiation on the $-z$ face

The first demonstration of AOP by c. w. laser irradiation was carried out on the polar z-faces of LN crystals using a frequency doubled argon ion laser source (244 nm) [67]. The initial observation of local etch frustration along the UV-irradiated tracks on the $-z$ face of the crystal [66] led to the further PFM investigation which confirmed local domain inversion. Further experiments revealed that AOP on the $-z$ face can also be observed for UV wavelengths up to 305 nm. The quality of the domain inversion was found to be a function of the irradiating laser intensity. This can be seen in Fig. 19 for three AOP domains generated in CLN with different laser powers (but fixed laser spot diameter

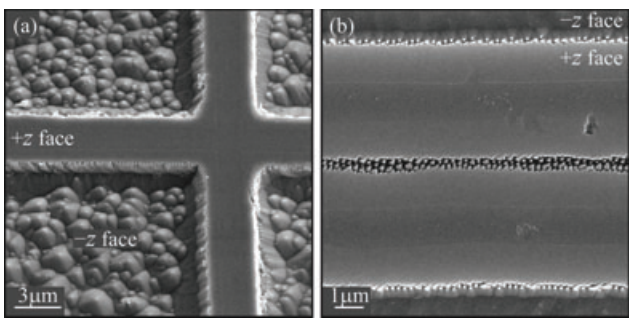

Figure 18 (a) Crossed poling-inhibited line domains with no indication of interaction with each other. (b) Two poling-inhibited line domains close to each other with submicron separation.

Table 5 Results of all-optical poling of LN crystals from the literature. λ = wavelength; C/P = c. w./pulsed laser; IT = intensity or peak intensity for pulsed laser (order of magnitude); ″ = same reference as the row above.

Crystal	λ [nm]	C/P	IT [W cm^{-2}]	Depth [μm]	Ref.
		$-Z$ FACE C. W. LASER IRRADIATION			
CLN	244	c. w.	10^5		[66]
CLN Fe:CLN Ti:CLN	244	c. w.	10^5	~ 1	[67]
		$+Z$ FACE C. W. LASER IRRADIATION			
CLN Fe:CLN Ti:CLN	244	c. w.	10^5	10^{-2}	[67]
		X, Y-FACE C. W. LASER IRRADIATION			
CLN Mg:CLN	275	c. w.	10^5	1.5	[68]
		$-Z$ FACE PULSED LASER IRRADIATION			
CLN	248	500 fs	10^{12}		[69]
LN	248	15 ns	10^6		[70]
CLN	248	20 ns	10^6		[71]
CLN	248	20 ns	10^6		[72]
CLN	308	25 ns	10^7		[73]
CLN	248	20 ns	10^7		[46]
		$+Z$ FACE PULSED LASER IRRADIATION			
CLN	248	20 ns	10^{7-8}	2	[74]
CLN	298–306	7 ns	10^{7-9}	2	″
CLN	308	25 ns	10^7		[73]
CLN	266	10 ns	10^{6-7}		[75]
CLN	298	7 ns	10^7		[46]
CLN	308	25 ns	10^7		[76]
CLN	10.6 μm	120 μs	10^{3-4}		[77]
CLN	266	4 ns			[78]
CLN Mg:CLN	308	25 ns	10^7	10	[79]
CLN Mg:CLN	10.6 μm	200 μs	10^4	10	″

~ 3 μm). At lower intensity (a,b) the domain inverted area consists of closely packed nano-domains which merge to form a continuous domain in c at an increased intensity close to the surface damage threshold (seen by the thermo-induced cracks).

Piezoresponse force microscopy (PFM) was also used to investigate the formation of AOP domains. For this purpose UV laser tracks were written on the surface of a PPLN sample, thereby analyzing in a single experiment the impact of the laser irradiation on both polar faces of LN. Figure 20a shows the topography where the surface damage owing to the horizontally written laser tracks is clearly seen. The results of the PFM scan acquired simultaneously are presented in Fig. 20b. The contrast levels in the PFM image can be directly attributed to the polarity of the surface, i. e., bright for a $+z$ and dark for a $-z$ face. The vertical pattern shows the initial PPLN structure. Note that the AOP domains exhibit the same contrast level as the $+z$ face domain from the PPLN structure. From this experimental result, it can be stated that in AOP only a $-z$ face is readily poled, and a $+z$ face stays unchanged.

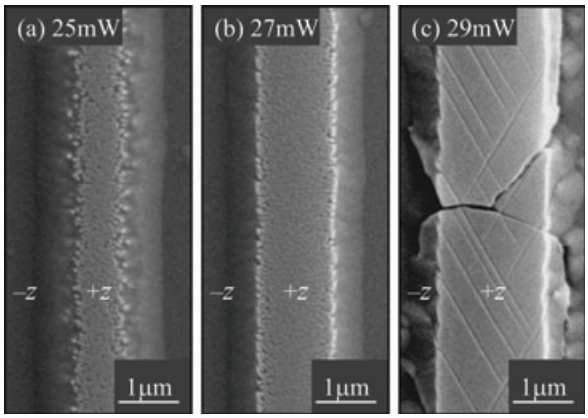

Figure 19 SEM images of etch frustrated tracks corresponding to AOP domains formed on the $-z$ face of an undoped CLN crystal after irradiation with a focused UV laser at 244 nm. (a,b) Assembly of AOP nano-domains. (c) Continuous domain achieved at higher intensity. Replotted from [67].

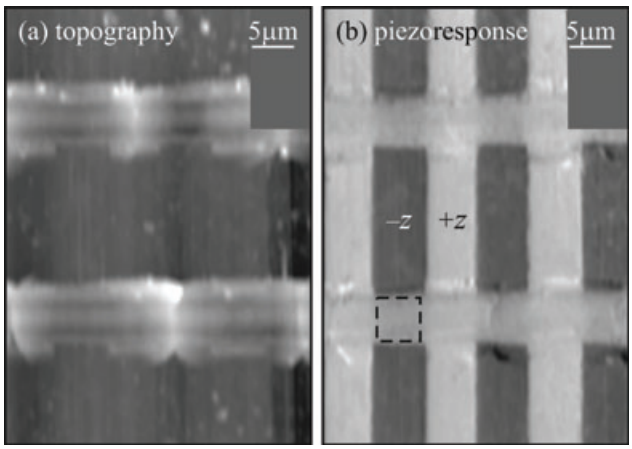

Figure 20 (a) Topography and (b) PFM piezoresponse of 244 nm UV written lines over PPLN. PPLN domains run vertically in the images and UV written lines run horizontally. In the PFM image $-z$ domains appear black and $+z$ domains appear white. UV irradiation is seen to invert $-z$ areas of PPLN as indicated by the dashed square in (b). Replotted from [67].

Irradiation on the $+z$ face

The above statement, that the $+z$ face stays unchanged in an AOP process needs further analysis. Indeed, HF etching

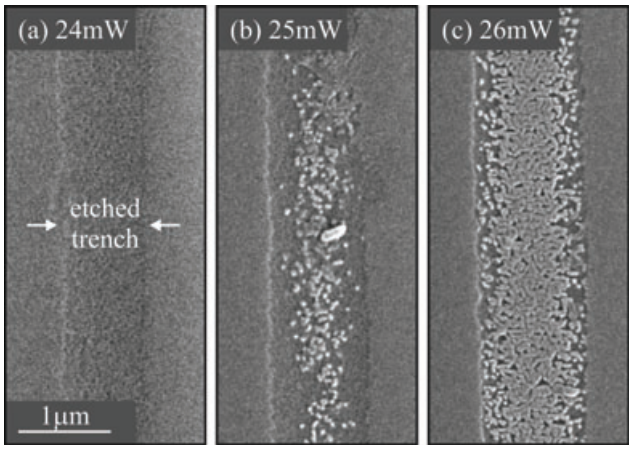

Figure 21 SEM images of HF acid etched $+z$ faces of undoped CLN that carries 244 nm UV written tracks. The lines were written with 0.1 mm s^{-1} writing speed, $\sim 3\,\mu$m beam diameter, and increasing writing power from (a) 24 mW to (c) 26 mW indicated. The range of etched shallow trench in (a) (corresponding to the written track) is indicated by the arrows. The length bar for (a) also applies to (b) and (c).

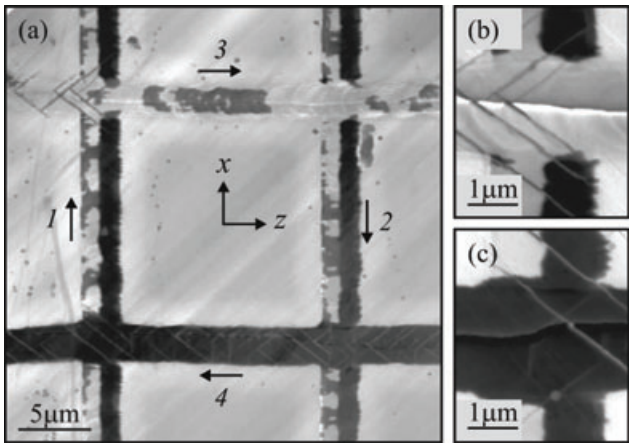

Figure 22 (a) PFM image of AOP domains obtained on a y-cut LN sample. The UV tracks are written along z- and x-directions as indicated by the arrows numbered in chronological order using the 275 nm line of an argon ion laser. (b) Magnified overlapping region between tracks *2* and *3*. (c) Magnified overlapping region between tracks *1* and *4*. Replotted from [68].

of a $+z$ face after AOP showed the existence of domain-inverted trenches corresponding to the previously UV irradiated tracks. The domains typically exhibit nanometer sized features (Fig. 21b,c) similar to the nano-domains on the $-z$ face observed in AOP (Fig. 19a) [67]. The depth of these trenches was determined to be of order of 10–20 nm only. This explains why they were not seen in the PFM image (Fig. 20b): The depth sensitivity of PFM imaging is $\sim 1.7\,\mu$m, and an ultra-thin layer of a few 10's of nm does not substantially alter the PFM contrast level [36]. Within a full-contrast PFM image, exhibiting bulk domains of both orientations, such a shallow domain-inverted surface layer cannot be resolved.

Irradiation on the x- or y-face

Finally, it has been shown recently that AOP domains can form also on the x- and y-faces of the crystal [68]. In this case it was observed that the writing direction of the UV irradiated tracks had a great impact on the AOP domain formation process. The PFM image in Fig. 22 shows the AOP domains formed on an y-cut crystal by scanning a UV laser ($\lambda = 275$ nm) along the directions indicated by the arrows and in the chronological order indicated by the numbers. As can be seen in Fig. 22a a domain inversion of the full width occurs only when the laser beam is scanned parallel to the z-direction and towards the $-z$ face (track *4*) while scanning towards the $+z$ face results in no domain at all (track *3*). The tracks *1* and *2* which are written along the x-direction show the formation of AOP domains with half the width of the laser-irradiated track. This can be clearly observed when comparing tracks *1* and *2* with track *4*. Figure 22b and c show enlarged views of the overlapping region between tracks.

4.2.2. AOP using pulsed laser irradiation

In this section we present results from experiments performed with pulsed laser irradiation whereby the controlled patterning of the domains was performed by using either an amplitude or a phase mask. In a different set of experiments, self-organized domain patterns were generated by homogeneous irradiation of the LN crystals.

Irradiation on the $-z$ face

A decade ago, pulsed UV laser irradiation on the $-z$ face was observed to alter the HF-etching behavior of LN crystals, whereby the laser pulses of 248 nm with pulse durations of 500 fs [69], and 15–20 ns [70–72] were utilized. It was found that using large fluence below the ablation threshold always resulted in non-continuous structures consisting of submicron features. Figure 23a shows an example where UV-exposure was performed through an absorption mask with $\sim 30\,\mu$m hexagonal openings. The inner part

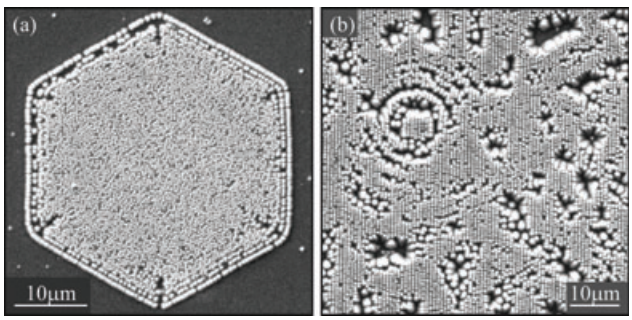

Figure 23 SEM images of etch frustrated patterns generated by illumination with 248 nm pulsed laser light. In (a) the laser beam was structured using a hexagon absorption mask. In (b) a phase mask was placed directly above the crystal. Replotted from [71].

consists of arbitrarily distributed nano-sized features, all exhibiting a similar size of ≈ 200 nm diameter. At its circumference, a quasi continuous frame has formed which is nearly two-rowed all around. The outer row has a width of about 500 nm and seems composed of merged single features. Obviously the individual features followed the interference light-pattern owing to the diffraction at the edges of the hexagonal openings. This effect can be utilized for the formation of ordered structuring as will be shown below.

The nano-sized featuring can be transferred into an ordered structure using a phase mask as is shown in Fig. 23b. Here the vertically aligned stripes are composed of single features exhibiting a size of ≈ 700 nm diameter. At many places, however, larger structures of merged domains can be seen. They are caused by diffraction patterns originating from dust particles that remained on the phase mask which was placed in close proximity to the $-z$ face of the crystal. This disturbing effect can be avoided when using a clean-room environment for the experiments.

In order to support the presumption that the topographical features obtained by HF-etching shown in Fig. 23 are caused by domain-inverted areas, PFM-investigations were performed of a sample irradiated with the help of the phase-mask. Figure 24 shows a SEM image of the topography a and the piezoresponse b. Note that the two images in Fig. 24 were not recorded at the same position of the crystal. It can, however, be seen that the grainy topographical structure observed in the SEM image is reflected in the PFM image, the size of the individual features being same. The etch-resistant features can thus be attributed to domain inverted structures. The depth of the individual sub-µm-sized domains, however, cannot be concluded from this PFM image. This would have required a bulk domain present in the same image section to allow for the quantitative comparison of the PFM-contrast, which was not available in this particular sample.

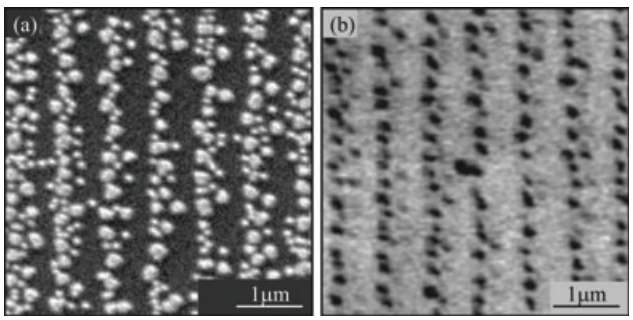

Figure 24 (a) SEM image of an irradiated (with a phase mask) and etched $-z$ face, showing the etch frustrated grating structure. (b) PFM image of an unetched sample exposed under similar condition as (a). Replotted from [72].

Investigations performed with different fluences of the irradiating laser beam showed that the density of the etch resistant features increases with increasing laser fluence. This is seen in Fig. 25 where a sequence of exposures (with increasing laser fluence) was carried out using a phase mask for generating a periodic intensity pattern. The topography

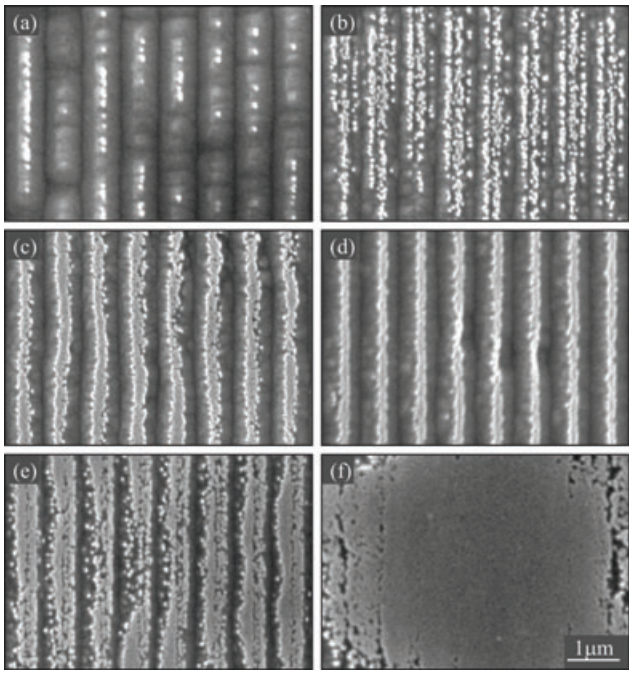

Figure 25 SEM micrographs showing progressively more merging of UV-induced domains formed via 10-pulse illumination with $\lambda = 248$ nm light through a phase mask by increasing the fluence of each spot: (a) 340, (b) 370, (c) 400, (d) 430, (e) 460, (f) 490 mJ cm^{-2}. The domain structures are revealed by brief HF acid etching. The length bar in (f) applies to all images. Replotted from [46].

shows a gradual densification of the etch resistant features. Low fluence results in individual domains within the irradiated areas, seen as the bright spots in a. Increasing the fluence first leads to an increase of the densities of individual domains in b until forming a continuous line (c and d). Further increase of the fluence leads to a widening of the lines e and for a laser fluence of 490 mJ cm^{-2} in f results in a fully merged structure [46]. However, at such high values of the laser fluence there is significant damage of the surface (ablation) which makes the identification of etch resistant features difficult hence the results become inconclusive.

Irradiation on the $+z$ face

When homogeneously irradiating the $+z$ face of LN crystals with pulsed laser UV light (248–308 nm) a very interesting behavior can be observed, namely the spontaneous formation of distinct self-organized ferroelectric domain structures [74,75,79]. As an example Fig. 26a shows such a structure obtained by using $\lambda = 298$ nm laser pulses whereby the intensity was above the ablation threshold. The domains are found to follow without exception the three identical y-axes of the crystal, as can be seen in the 2D Fourier transform shown in the inset of Fig. 26b. Interestingly the filling of the available surface area with the line-like domains takes place without crossing their paths [46,74]. The individual lines are found to exhibit a width of ≈ 160 nm (Fig. 26c) irrespective

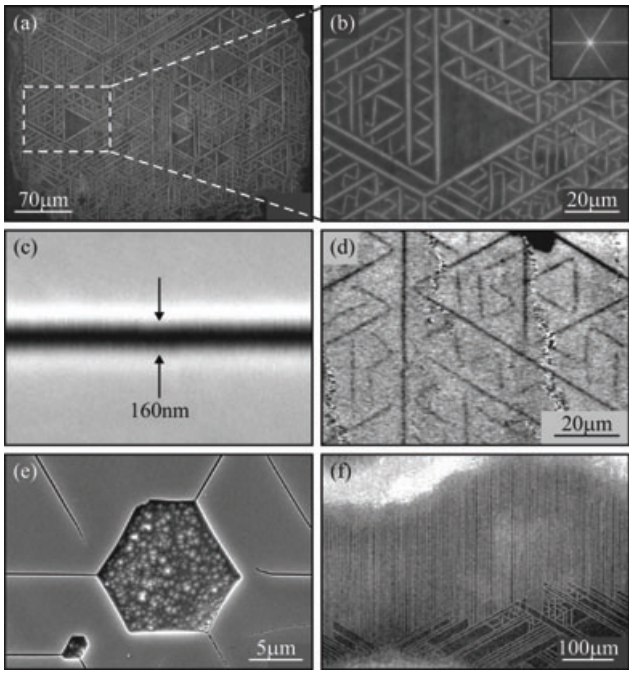

Figure 26 (a–c) SEM images of the $+z$ face of undoped CLN crystals that have been irradiated with a pulsed laser at 298 nm above the ablation threshold and subsequently etched in HF acid for 30 min. Etched trenches align along the y-axes. (b) An enlarged image of the region enclosed by the dashed rectangle in (a). The inset in (b) shows the 2D Fourier transform of the etched pattern, clearly demonstrating the three-fold symmetry. (c) Detail from (a), showing a single continuous etched line feature. Replotted from [46]. (d) PFM image showing piezoresponse contrast which is effectively identical to those produced through HF etching in (a-c). Replotted from [74]. (e) SEM image of line features in Mg:CLN, showing self-organized lines spreading or being deflected from the corners of a bulk domain. Replotted from [46]. (f) Phase mask has been used for periodic domain patterning with pulsed laser at 266 nm. Replotted from [75].

of the intensity used. The density of the features, however, increases with the laser intensity.

Again in order to support the presumption that the topographical features obtained by HF-etching shown in Fig. 26a–c are caused by domain-inverted areas, PFM-investigations were performed. The piezoresponse of an unetched sample is shown in Fig. 26d revealing the very same features as were observed by SEM imaging of the differentially etched samples. The topography acquired simultaneously (not shown) exhibited no contrast at all.

The impressive quasi-perfect line-like domains now point towards an obvious question: is there a way to control the self-organized formation of the domains in order to generate useful domain patterns? Or to put the question in another way: can one structure those self-organized domain patterns? Within this framework the effect of bulk domains which were present in the crystal before pulsed laser irradiation was investigated. It was thereby shown by [46] that micron sized domains in Mg:CLN crystals act as seeds for the propagation of all optically poled domains obtained in pulsed irradiation experiments. This is illustrated in Fig. 26e where the etched trenches, i. e., the AOP domains, stem from the three apices of the hexagonal (bulk) domain and propagate along the y-directions of the crystal which are indicated by the orientation of the hexagonal domain.

In an attempt to control the formation of the self-organized domains on a large scale, CLN samples were exposed to laser pulses using a phase mask which was oriented in such a way as to produce a grating aligned along one of the y-directions of the crystal [75]. The attempt was successful to some extent as shown in Fig. 26f: as the majority of the features were aligned along the grating lines however, inhomogeneities in the irradiating conditions cause divergence of the domain formation to the other two y-directions as can be seen in the bottom part of the image.

Finally, the depth of the domains is an important issue in terms of their applicability. Investigations of [74] revealed a depth of the order of $\sim 2\,\mu$m. However, y-face etching experiments by [79] showed that depths of several tens of microns are possible.

4.3. Discussion of UV laser-induced poling

A summary of the dominant observations on UV laser-induced poling is presented below:

1. c. w. laser irradiation
   a) $-z$ face: all-optical poling, i. e., domain inversion in the irradiated area.
   b) $+z$ face: poling inhibition, i. e., the resistance of a previously irradiated area to subsequent electric field poling.
   c) x, and y-faces: all-optical poling, i. e., domain inversion in the irradiated area. Dependence of the domain formation on the writing direction of the laser track.
2. Pulsed laser irradiation
   a) $-z$ face: all-optical poling, i. e., domain inversion in the irradiated area. Formation of arbitrarily distributed sub-μm-sized domains.
   b) $+z$ face: all-optical poling, i. e., domain inversion in the irradiated area. Formation of self-organized line-shaped domains of sub-μm-width.

Before discussing the physical effects behind all types of UV laser-induced poling we will briefly review the properties of LN relevant for the following. The first point concerns the value of the coercive field E_c, where changes of the crystal stoichiometry (and thus the Li content in particular) are known to cause significant changes in value of the coercive field [80]. Basically E_c increases with increasing lithium deficiency, and consequently, CLN exhibits a much larger value for E_c than SLN. Hence a local variation of the Li-concentration is mirrored by an equivalent local variation of E_c.

A further point that needs to be analyzed is the effect of highly absorbed deep-UV laser irradiation on the crystal properties. Irradiation of LN with deep-UV light leads a priori to a heating of the crystal's surface since the absorption length is $\ll 100$ nm only. Using a high laser intensity, it is thereby possible to reach temperatures close to or

even exceeding both the Curie and the melting temperature ($T_{\mathrm{Curie}} = 1415\,\mathrm{K}$ and $T_{\mathrm{melt}} = 1530\,\mathrm{K}$). At such high temperatures the lithium becomes mobile as its activation energy is 1.55 eV [81, 82]. Note that ferroelectrics at elevated temperatures exhibit a lower E_{c} (that vanishes by definition at $T = T_{\mathrm{Curie}}$).

Local irradiation of a crystal leads to heating of a very restricted volume at the crystal surface which in turn results in steep temperature gradients at the border of the heated volume [83]. Under these extreme conditions lithium ions become mobile and diffuse away from the center of the laser spot under the influence of the temperature gradients [65]. A local lithium deficiency leads to the local increase of both the coercive field and the extraordinary refractive index [84]. The obtained refractive index profile enabled the direct writing of optical waveguides [85, 86] with preserved high nonlinearity [87].

The last point to be considered is the pyroelectric effect that occurs during the cooling stage, following laser irradiation. The build-up of an electric field following the laser irradiation (when no light-induced free charge carriers are present to compensate for any E-field distribution) might produce an electric field, therefore assisting the lithium migration process [67].

For all experiments carried out with a c. w. laser it was found that the domain-inverted area roughly overlaps with the range of highly elevated temperature caused by the irradiating laser. It was also observed that all experiments required a similar laser intensity for successful domain formation, namely an intensity that allows for reaching temperatures close to T_{Curie} or T_{melt}. It seems therefore natural that the heat-profile causes the changes in the crystal property required for poling.

For all-optical poling on the $-z$ face, the electric field caused by the pyroelectric effect can be the origin for domain formation, as the E-field during cooling points in exactly the required direction [67]. All-optical poling on the x- and y-faces, however, cannot be explained by the same mechanism. Indeed, it seems that the direction of polarization follows a temperature gradient in the crystal [88]. Using this assumption, the dependence of the domain formation on the writing direction can also be explained.

Poling-inhibition which was found to take place on the $+z$ face only can be explained by the lithium diffusion out of the laser irradiated area [65]. The resulting coercive field distribution, enhanced at the center of the laser beam and lowered at its sides, could be confirmed by local poling using scanning probe microscopy. In addition annealing experiments revealed that the effect of the UV laser irradiation on poling inhibition survives temperatures up to 250 °C. This supports further the explanation of poling inhibition via the lithium redistribution as other species (hydrogen in particular) are mobile at this temperature and would have compensated for any residual electric field.

It was proposed in [79] that the formation of AOP domains on the $+z$ face of CLN crystals by pulsed laser illumination in Sect. 4.2.2 is due to the pyroelectric field acting during the cooling stage that follows the termination of the laser pulse, taking into account the screening effect retardation. The proposed mechanism is supported by similar results from infrared (200 µs, 10.6 µm) illumination experiments [79].

The effects which are induced by pulsed UV laser irradiation can also be explained to some extent by the mechanisms that were proposed in the previous paragraphs. However, in the pulsed irradiation case the heating stage of the process is determined by the pulse duration (which is $\sim 500\,\mathrm{fs}$ to 200 µs) while in the c. w. case it was determined by the dwell time of the beam during scanning and could be substantially longer. Hence for each pulse there is a corresponding heating-cooling cycle of the same duration. As a consequence the first heating-cooling cycle corresponding to the first pulse can change the domain distribution of the surface which means that subsequent pulses 'see' a modified surface. This might be the reason why the AOP features which are observed on the $-z$ face cannot become continuous at low intensities (Fig. 23). At higher laser intensities, the AOP features start merging. However, at these intensities severe surface damage (laser ablation) occurs which reduces the utility of the method.

5. Micro-structuring

The formation of surface microstructures on lithium niobate crystals is of high technological interest and has been the subject of recent research activity. Surface microstructuring methods that have been employed for this purpose include focused ion beam (FIB) [89–91] and reactive ion etching (RIE) [92, 93]. While both methods can achieve high quality microstructures, they pose limitations in terms of fabrication area and aspect ratio of the achievable structures. In this last section, we will discuss the possibilities of fabricating lithium niobate superstructures starting from ferroelectric domain patterns. The key element in the procedure, assuming that an appropriate domain pattern is present, is long-term, up to several tens of hours of differential etching in hydrofluoric acid (HF) mixtures: the $-z$ face etches at a rate of $\gamma_z \approx 1\,\mu\mathrm{m\,h^{-1}}$) whereas the acid does not attack the $+z$ face at all [34]. Extended HF etching has proven to be a powerful method for surface micro-structuring of LN crystals as has been demonstrated in [94, 95]. Fabrication of micro-structures, starting from domain patterns, such as alignment grooves [96], ridge waveguides [8, 97], and even free standing single crystal micro-cantilevers [7] have been demonstrated so far using the patterned domains. The effect of refractive index increase owing to UV-irradiation, discussed previously (Sect. 4.3), together with poling inhibition, followed by deep HF-etching allowed for the formation of ridge waveguides [8].

In addition to the differential etching of the z-faces, the $\pm y$ faces also etch differently, however with much smaller etching rates ($+y$ face: $\approx 1/6\,\gamma_z$ and $-y$ face: $\approx 1/5\,\gamma_z$) [98]. Consequently an initial circular shape transforms into a triangular shape owing to the *3m* crystal symmetry. The x-face etches at a much slower rate ($\approx 1/30\,\gamma_z$) compared to y- and z-face etching. The etching properties of the different faces

of LN lead to a further faceting of the micro-structures during a long-term etching process. The strongly different etch rates between the $-z$ face and the two y-faces, however, allow for undistorted domain curvatures for micro-structures during etching with height restricted to a few microns. Examples of curved domain structures are shown in Fig. 27 with very different radii of curvature.

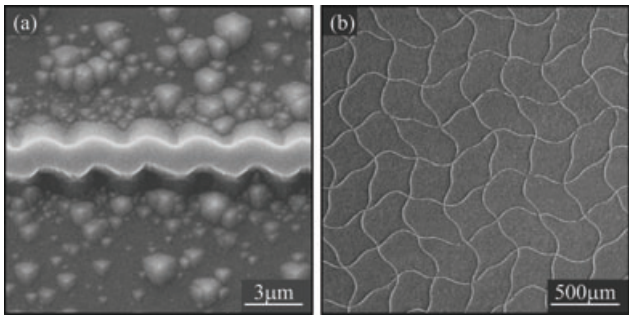

Figure 27 SEM images of ridge structures corresponding to (a) etched AOP domain track created by a modulated beam, and (b) etched PI domain webbing patterns.

In order to realize arbitrary surface micro-structures, free of any crystallographic restrictions, light-mediated processes for fabricating the underlying domain patterns is appreciated as they are faithful replicas of the irradiating light distribution. Note that both poling inhibited (PI) as well as all optically poled (AOP) domains exhibit the proper domain face configuration to result in ridge structures of any previously irradiated traces.

Ridge structures can function as optical channel waveguides which can accommodate tight curvatures due to the large dielectric contrast between the bulk material and air. An example is shown in Fig. 28 where a PI domain pattern was used to fabricate a set of circular ring superstructures connected by linear segments. In order for such structures to guide light it is also necessary for the ridge to exhibit a higher refractive index with respect to the underlying bulk. In LN this is commonly produced by diffusion of titanium [99]. However, it was shown in [8] that during the UV exposure (which constitutes the first part in the PI process) the refractive index is increased in the irradiated area, which is sufficient to provide the vertical optical confinement for the formation of a ridge waveguide.

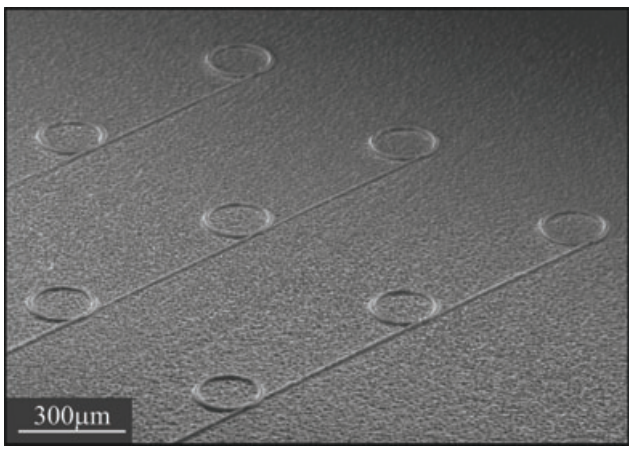

Figure 28 SEM image (tilted at 60°) of ring superstructures connected by linear segments produced by etching of PI domains in a CLN crystal.

The light-mediated domain inversion methods which were outlined in the previous sections commonly produce domains which have limited depth, of the order of a couple of microns only. However, even a very shallow $+z$ face domain can act as an absolute etch-stop, thus allowing the creation of structures which are much deeper than the depth of the initial domain. This can be seen in Fig. 29 where the vertical slabs have a height of $\sim 35\,\mu$m which is roughly 15 times larger than the depth of the initial PI domains. Since the domains which preceded the slabs were aligned along the y-axis of the crystal, the side walls visible in the SEM image correspond therefore to x-faces (which etch much slower that $-z$ face). Obviously this orientation allows for the generation of ridge structures of extraordinary aspect ratio.

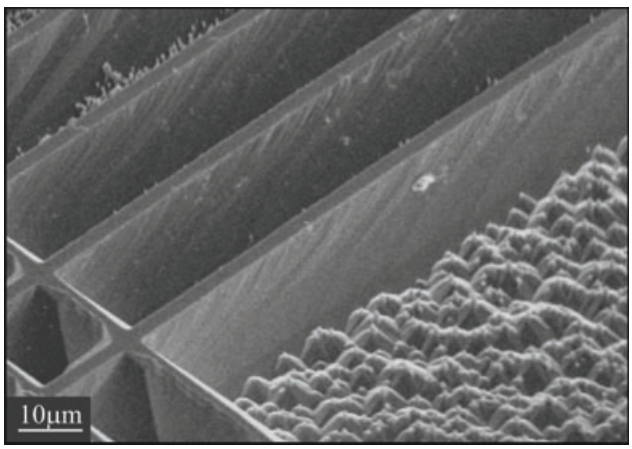

Figure 29 SEM image (tilted at 45°) of large aspect ratio surface structures in undoped CLN produced by extended etching of PI domains for tens of hours. The long sections of the slabs are aligned along the y-axis of the crystal thus producing x-face sidewall surfaces which etch much slower than $-z$ face.

Domains exhibiting walls which are not aligned along a y-axis result in complex micro-structures during long-term etching since differential etching between opposite y-faces takes place. Even more domains of limited depth develop complex shapes when the etch depth reaches the depth of the inverted domain. At this stage, the slope of the sidewalls reverses, thus creating undercuts as shown in Fig. 30a–c where the micro-pillars emerged from initially circular domains.

LN crystals are primarily used for applications in photonics, and the quality of the optical interfaces is therefore a crucial factor in device fabrication as any surface roughness results in optical loss. Besides high-quality polishing, a method for surface smoothening consists of its melting,

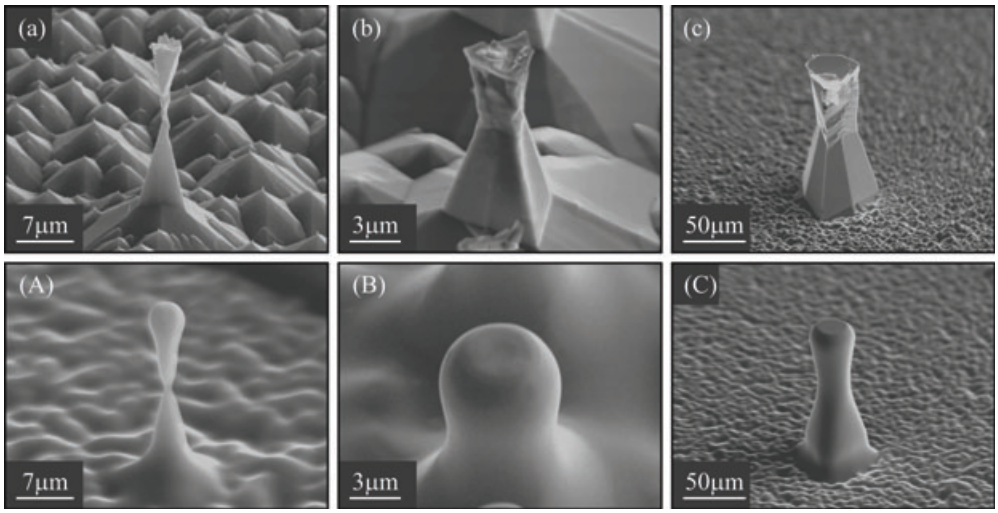

Figure 30 SEM images tilted at 60°. (a-c) Initial structures developed from HF etching of $+z$ face LAP surface circular domains with various diameters from (a) $\sim 5\,\mu$m to (c) $\sim 40\,\mu$m. (A-C) Ultra-smooth resonator structures after thermal treatment of the corresponding initial structures shown in (a-c). Replotted from [100, 101].

thereby allowing the surface tension to reshape the surface and eliminate any roughness. This method has been applied to glass materials and has also been successfully adopted to glass micro-structures where whispering gallery resonators with record high Q factors ($\sim 10^{10}$) have been demonstrated [102]. Recently Ying et al. [103] demonstrated that surface tension reshaping can also be applied to LN micro-structured surfaces. Here the LN samples were subjected to temperatures just below the melting point of the crystal. At such temperatures the surface melts preferentially while the bulk of the crystal remains solid. The melted surface is reshaped by the surface tension and re-crystallizes, seeded by the bulk during cooling, therefore maintaining in this way the single crystal nature of the material.

The SEM images which are shown in Fig. 30A–C correspond to the surface tension reshaped structures of a–c. The reshaped micro-structures have an ultra-smooth surface, and due to the presence of an undercut in the original micro-structure, exhibit a shape that is suitable to support whispering gallery modes. Extended etching of undercut structures like the ones shown in Fig. 30a–c leads to the elimination of the top part of the structure thus forming ultra-sharp single domain micro-tips. An array of such micro-tips is shown in the SEM image of Fig. 31a. Surface tension reshaping of such micro-structures leads to the formation of a micro-lens array as shown in Fig. 31b.

In most applications, the etched backgrounds are not of concern. However, sometimes a smooth background might be required, e. g., in the case of shallow ridge waveguides where the roughness of backgrounds can lead to the loss of the guiding. Improvements in HF etching can be achieved either by adding ethanol to HF-HNO_3 mixture [104–106], or using vapour HF etching. Hu et al. has found that by adding ethanol to HF-HNO_3 mixture with volume ratio of 1:7 at 22 °C, the etched surface can be much smoother than without ethanol as shown in Fig. 32a and b of the difference. The alcohol reduces the surface tension of the etchant and suppress the generation of hydrogen bubbles in the etching process; thus, a smooth etched surface could be obtained [106]. Additionally, using 50 °C vapour HF etching can also provide a smooth background.

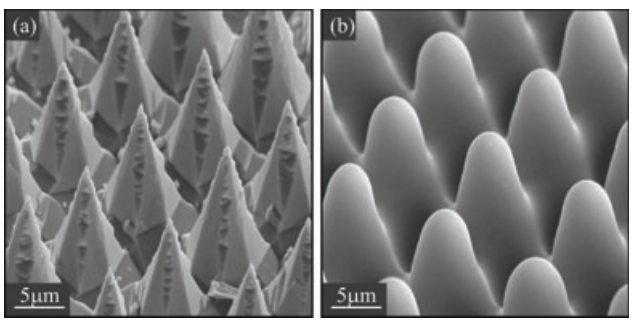

Figure 31 SEM images tilted at 60°. (a) Tip array in undoped CLN crystal fabricated by long etching of PI circular domains so that the top PI domain of $+z$ face has been totally etched away. (b) Micro-lens array structures fabricated by thermal treatment of the tip array in (a).

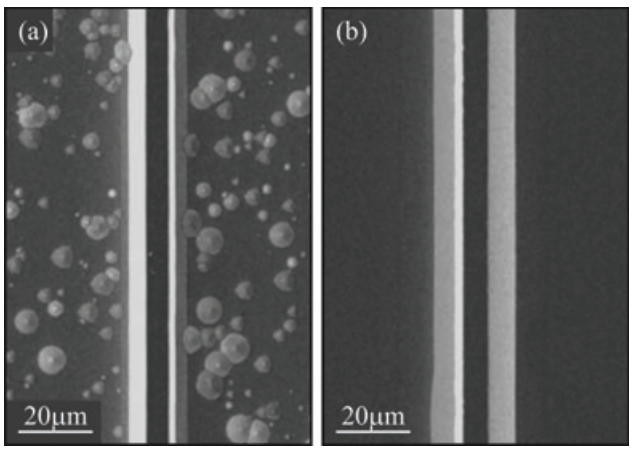

Figure 32 SEM images for comparison of two etched $-z$ surfaces. (a) A surface with a ridge etched by HF-HNO_3 without ethanol (the bright stripes along both sides of the ridge are the etched walls). (b) A smooth surface etched with ethanol. Replotted from [104].

6. Conclusions

The impact of irradiation with intense c. w. or pulsed laser sources on ferroelectric domain inversion in lithium niobate crystals has been reviewed here. It was shown that light from the deep-UV to the long-wavelength-IR spectral range can be used to modify the coercive and the nucleation field or even directly induce domain inversion in the absence of any externally applied electric field (for deep-UV wavelengths). Laser irradiation provides thus an alternative route for spatially selective domain inversion that eliminates the need for micro-structured electrodes in electric field poling. When visible and near-IR laser sources are used for the irradiation of the crystals, the physical origin of the observed effects (light assisted poling (LAP) and latent LAP) has been attributed to the combination of photo-induced space charge fields, screening of the surface defects, and modification of the crystal's defect structure. For UV laser sources with wavelengths lying within a spectral region where the crystals show very strong absorption (for deep-UV and long-wavelength-IR wavelengths), the observed effects (poling inhibition, all-optical poling) were attributed to the diffusion of lithium ions due to steep temperature gradients assisted by the pyroelectric effect. Laser-mediated domain inversion methods produce ferroelectric domain patterns of limited depth which nevertheless can be used for nonlinear optics in waveguides as their depth is sufficient to overlap with optical waveguide modes.

However, irrespectively of their depth these domains can be used as etch stops for the fabrication of surface microstructures. The fabrication of high aspect ratio structures originating from such shallow domains was demonstrated here. Etching of inverted domains with limited depth produces structures with undercuts which after surface reshaping at elevated temperatures become sufficiently smooth to be suitable for the confinement of light in whispering gallery modes. Light-mediated domain inversion processes seem to be immune to the domain shape restrictions exerted by the symmetry of the crystal thus allowing the fabrication of curved domain shapes which are suitable for photonic applications.

Today the dominant method for ferroelectric domain engineering is still based on the direct application of an external electric field. However, laser-mediated methods, although at their infancy, can provide clear advantages, for example, in the fabrication of waveguide nonlinear devices or in cases where the crystal symmetry and the domain proximity is a restrictive factor. Additionally, the significant reduction of the coercive field could provide a route for the domain engineering of thicker crystals for high peak power nonlinear applications. Finally, the processes which have been outlined in this paper have contributed to the better understanding of the domain inversion mechanism, have given insight about laser-material interactions, and have provided a very powerful tool for the surface microstructuring which can well expand the applicability of this technologically important optical crystal.

Acknowledgements. The authors would like to acknowledge the contribution of Dr. I. T. Wellington, Dr. J. G. Scott, Dr. M. C. Wengler, Dr. T. Jungk, Dr. A. Hoffmann, and Prof. K. Buse. They are also grateful to the Engineering and Physical Sciences Research Council, UK, for research funding under Grant No. EP/C515668 and PhD-Plus, to the European commission for funding within the framework of the STREP 3D DEMO, to Materials World Network (MWN) grant funded by the Deutsche Forschungsgemeinschaft and the U. S. National Science Foundation (Grant No. NSF-DMR 60 0602986), and to the Deutsche Telekom AG.

Received: 1 April 2011, **Revised:** 14 July 2011, **Accepted:** 16 August 2011

Published online: 26 September 2011

Key words: Lithium niobate, ferroelectrics, domain engineering, micro-structuring.

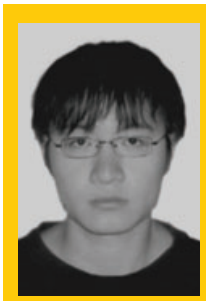

Charlie Y. J. Ying received his B. Sc. (hons.) in applied physics from City University of Hong Kong in 2007. In 2010 he obtained Ph. D. degree from the Optoelectronics Research Center at the University of Southampton for his work on light-assisted domain engineering, waveguide fabrication, and microstructuring of lithium niobate. He is currently working under EPSRC PhD-Plus fellowship in the same group investigating single crystalline lithium niobate micro-resonators. His research interests include domain engineering, microstructuring of ferroelectrics, and integrated optics.

Alistair C. Muir obtained his bachelors degree in physics at the University of Southampton in 2004. Upon completion of his undergraduate studies he remained at the University of Southampton to study for his Ph. D. at the Optoelectronic Research Centre (ORC). He completed his Ph. D. in May 2008 and joined the Centre for Photonics and Photonic Materials at the University of Bath in July 2008. His research interests include lithium niobate and the influence of UV light, non-linear optics and photonic crystal fibres.

Christopher E. Valdivia received his Ph. D. from the Optoelectronics Research Centre of the University of Southampton, UK, in 2007. Subsequently, he completed a postdoctoral fellowship studying high-efficiency multi-junction III-V semiconductor solar cells and concentrated photovoltaics in the Centre for Research in Photonics at the University of Ottawa, Canada. Continuing in this field, he joined the research and development department of Cyrium Technologies Inc. in 2010.

Hendrik Steigerwald studied physics at the University of Marburg, Marburg, Germany, and at the University of Bonn, Germany, where he obtained his final degree in 2007. He is currently working toward the Ph. D. degree in ferroelectric domains in photorefractive crystals in the group of K. Buse at the Physics Department, University of Bonn.

Collin L. Sones received the B. Sc. degree in physics from B. K. M Science College, South Gujarat University, Surat, India, in 1989, the M. Sc. degree from the Department of Physics, South Gujarat University, in 1991, and the Ph. D. degree from the Optoelectronics Research Center (ORC), University of Southampton, Southampton, U. K., in 2003. He joined the Department of Physics, J. P. Arts and Science College, Bharuch, India, as a Lecturer in 1991. After the Ph. D. degree, he joined the ORC, University of Southampton, as a Research Fellow, where he is currently employed as a Senior Research Fellow. At the ORC, his research has been focused at developing effective techniques for micro domain engineering of nonlinear ferroelectric materials for the applications in fields as different as microelectromechanical systems and guided-wave integrated optical devices. His current activity involves the use of the laser-based printing method, Laser-Induced Forward Transfer, for application-driven functional devices.

Robert W. Eason is a professor of Optoelectronics and deputy head of school in the Optoelectronics Research Centre, University of Southampton, where he has been involved in optoelectronics research for more than 20 years. He received the degree of D.Phil from the University of York in 1982, and has also worked at the Rutherford Appleton Laboratory, Didcot, UK, and the University of Essex, UK, where he was appointed as a new-blood lecturer in 1984. His research interests span optical and nonlinear optical materials, laser-material interactions, the growth and characterisation of optical thin films grown by pulsed laser deposition, optical waveguides and femtosecond laser technology and applications, particularly in the area of direct laser printing.

Elisabeth Soergel received her Ph. D. degree in physics from the Ruprecht-Karls-University in Heidelberg, Germany, in 1999 on the investigation of photorefractive crystals with scanning force microscopy. Subsequently, she was as a Postdoctoral Researcher at the IBM Research Laboratories, Rueschlikon, Zurich, Switzerland, investigating the possibilities for storage devices based on scanning tunnelling microscopy. Since 2001, she has been with the University of Bonn, Germany, where she got her habilitation in 2006, working on the subject of visualization of ferroelectric domains with piezoresponse force microscopy.

Sakellaris Mailis received his Ph. D. degree on signal processing with photorefractive materials in 1996 from the Physics department of the University of Crete in association with the Foundation for Research and Technology Hellas (FORTH). Apart from research on photorefractive crystals he has been investigating the photosensitivity of semiconducting oxide materials as well as direct laser micro-printing.

References

[1] W. Sohler, H. Hu, R. Ricken, V. Quiring, C. Vannahme, H. Herrmann, D. Büchter, S. Reza, W. Grundkötter, S. Orlov, H. Suche, R. Nouroozi, and Y. Min, Opt. Photon. News **19**(1), 24 (2008).
[2] R. S. Weis and T. K. Gaylord, Appl. Phys. A **37**(4), 191 (1985).
[3] E. L. Wooten, K. M. Kissa, A. Yi-Yan, E. J. Murphy, D. A. Lafaw, P. F. Hallemeier, D. Maack, D. V. Attanasio, D. J. Fritz, G. J. McBrien, and D. E. Bossi, IEEE J. Sel. Top. Quantum Electron. **6**(1), 69 (2000).
[4] D. Janner, D. Tulli, M. García-Granda, M. Belmonte, and V. Pruneri, Laser Photonics Rev. **3**(3), 301 (2009).
[5] G. D. Miller, R. G. Batchko, W. M. Tulloch, D. R. Weise, M. M. Fejer, and R. L. Byer, Opt. Lett. **22**(22), 1834 (1997).
[6] H. Gnewuch, C. N. Pannell, G. W. Ross, P. G. R. Smith, and H. Geiger, IEEE Photonics Technol. Lett. **10**(12), 1730 (1998).
[7] C. Sones, S. Mailis, V. Apostolopoulos, I. E. Barry, C. Gawith, P. G. R. Smith, and R. W. Eason, J. Micromech. Microeng. **12**(1), 53 (2002).
[8] C. L. Sones, P. Ganguly, C. Y. J. Ying, E. Soergel, R. W. Eason, and S. Mailis, Appl. Phys. Lett. **97**(15), 151112 (2010).
[9] M. Yamada, N. Nada, M. Saitoh, and K. Watanabe, Appl. Phys. Lett. **62**(5), 435 (1993).
[10] J. Webjörn, V. Pruneri, P. S. J. Russell, J. R. M. Barr, and D. C. Hanna, Electron. Lett. **30**(11), 894 (1994).
[11] S. Grilli, C. Canalias, F. Laurell, P. Ferraro, and P. D. Natale, Appl. Phys. Lett. **89**(3), 032902 (2006).
[12] H. Ishizuki, I. Shoji, and T. Taira, Appl. Phys. Lett. **82**(23), 4062 (2003).
[13] H. Steigerwald, F. von Cube, F. Luedtke, V. Dierolf, and K. Buse, Appl. Phys. B **101**(3), 535 (2010).
[14] C. Restoin, C. Darraud-Taupiac, J. L. Decossas, J. C. Vareille, J. Hauden, and A. Martinez, J. Appl. Phys. **88**(11), 6665 (2000).
[15] X. Li, K. Terabe, H. Hatano, and K. Kitamura, Jpn. J. Appl. Phys. **44**(51), L1550 (2005).
[16] M. Lilienblum, A. Ofan, A. Hoffmann, O. Gaathon, L. Vanamurthy, S. Bakhru, H. Bakhru, R. M. Osgood, Jr., and E. Soergel, Appl. Phys. Lett. **96**(8), 082902 (2010).
[17] G. Rosenman, P. Urenski, A. Agronin, Y. Rosenwaks, and M. Molotskii, Appl. Phys. Lett. **82**(1), 103 (2003).

[18] D. Xue, S. Wu, Y. Zhu, K. Terabe, K. Kitamura, and J. Wang, Chem. Phys. Lett. **377**(3), 475 (2003).
[19] V. Y. Shur, E. L. Rumyantsev, E. V. Nikolaeva, E. I. Shishkin, D. V. Fursov, R. G. Batchko, L. A. Eyres, M. M. Fejer, and R. L. Byer, Appl. Phys. Lett. **76**(2), 143 (2000).
[20] F. S. Chen, J. Appl. Phys. **40**(8), 3389 (1969).
[21] G. G. Zhong, J. Jin, and Z. K. Wu, J. Opt. Soc. Am. **70**(6), 631 (1980).
[22] D. A. Bryan, R. Gerson, and H. E. Tomaschke, Appl. Phys. Lett. **44**(9), 847 (1984).
[23] N. Iyi, K. Kitamura, Y. Yajima, S. Kimura, Y. Furukawa, and M. Sato, J. Sol. St. Chem. **118**(1), 148 (1995).
[24] Y. Furukawa, K. Kitamura, S. Takekawa, K. Niwa, and H. Hatano, Opt. Lett. **23**(24), 1892 (1998).
[25] Y. Furukawa, K. Kitamura, S. Takekawa, A. Miyamoto, M. Terao, and N. Suda, Appl. Phys. Lett. **77**(16), 2494 (2000).
[26] A. Péter, K. Polgár, L. Kovács, and K. Lengyel, J. Crysr. Growth **284**(1–2), 149 (2005).
[27] M. C. Wengler, U. Heinemeyer, E. Soergel, and K. Buse, J. Appl. Phys. **98**(6), 064104 (2005).
[28] H. Steigerwald, F. Luedtke, and K. Buse, Appl. Phys. Lett. **94**(3), 032906 (2009).
[29] C. L. Sones, M. C. Wengler, C. E. Valdivia, S. Mailis, R. W. Eason, and K. Buse, Appl. Phys. Lett. **86**(21), 212901 (2005).
[30] F. Kalkum, H. A. Eggert, T. Jungk, and K. Buse, Journal of Applied Physics **102**(1), 014104 (2007).
[31] M. C. Wengler, PhD thesis, Rheinische Friedrich-Wilhelms-Universität Bonn (2005).
[32] J. Li, L. Liu, Y. Liu, and C. Zhou, Microw. Opt. Technol. Lett. **26**(2), 89 (2000).
[33] M. Müller, E. Soergel, and K. Buse, Appl. Phys. Lett. **83**(9), 1824 (2003).
[34] C. L. Sones, S. Mailis, W. S. Brocklesby, R. W. Eason, and J. R. Owen, J. Mater. Chem. **12**(2), 295 (2002).
[35] M. Alexe and A. Gruverman (eds.), Nanoscale Characterisation of Ferroelectric Materials (Springer, Berlin, 2004).
[36] F. Johann, Y. J. Ying, T. Jungk, A. Hoffmann, C. L. Sones, R. W. Eason, S. Mailis, and E. Soergel, Appl. Phys. Lett. **94**(17), 172904 (2009).
[37] T. J. Yang, V. Gopalan, P. J. Swart, and U. Mohideen, Phys. Rev. Lett. **82**(20), 4106 (1999).
[38] T. J. Yang and U. Mohideen, Phys. Lett. A **250**(1–3), 205 (1998).
[39] S. Kim and V. Gopalan, Mater. Sci. Eng. B **120**(1–3), 91 (2005).
[40] V. Gopalan and T. E. Mitchell, J. Appl. Phys. **85**(4), 2304 (1999).
[41] P. Hou, Y. Zhi, and L. Liu, Appl. Phys. A **99**(1), 105 (2010).
[42] V. Dierolf and C. Sandmann, Appl. Phys. Lett. **84**(20), 3987 (2004).
[43] C. E. Valdivia, C. L. Sones, S. Mailis, J. D. Mills, and R. W. Eason, Ferroelectrics **340**(1), 75 (2006).
[44] P. T. Brown, G. W. Ross, R. W. Eason, and A. R. Pogosyan, Opt. Commun. **163**(4–6), 310 (1999).
[45] M. Fujimura, T. Sohmura, and T. Suhara, Electron. Lett. **39**(9), 719 (2003).
[46] C. E. Valdivia, PhD thesis, University of Southampton, Southampton (2007).
[47] M. C. Wengler, B. Fassbender, E. Soergel, and K. Buse, J. Appl. Phys. **96**(5), 2816 (2004).
[48] H. A. Eggert, F. Kalkum, M. C. Wengler, U. Heinemeyer, and K. Buse, Ferroelectrics **340**(1), 63 (2006).
[49] W. Wang, Y. Kong, H. Liu, Q. Hu, S. Liu, S. Chen, and J. Xu, J. Appl. Phys. **105**(4), 043105 (2009).
[50] H. Zeng, Y. Kong, H. Liu, S. Chen, Z. Huang, X. Ge, and J. Xu, J. Appl. Phys. **107**(6), 063514 (2010).
[51] A. Räuber, Current Topics in Material Science (North-Holland, Amsterdam, 1978).
[52] D. S. Li, D. A. Liu, Y. N. Zhi, W. J. Qu, L. R. Liu, and J. Zhang, Chinese Phys. Lett. **24**(4), 971 (2007).
[53] H. D. Liu, Y. F. Kong, Q. Hu, R. W. Wu, W. J. Wang, X. C. Li, S. L. Chen, S. G. Liu, and J. J. Xu, Chinese Phys. Lett. **24**(6), 1720 (2007).
[54] Y. Zhi, D. Liu, W. Qu, Z. Luan, and L. Liu, Appl. Phys. Lett. **90**(4), 042904 (2007).
[55] H. Zeng, Y. Kong, T. Tian, S. Chen, L. Zhang, T. Sun, R. Rupp, and J. Xu, Appl. Phys. Lett. **97**(20), 201901 (2010).
[56] Y. J. Ying, C. E. Valdivia, C. L. Sones, R. W. Eason, and S. Mailis, Opt. Express **17**(21), 18681 (2009).
[57] C. Y. J. Ying, PhD thesis, University of Southampton, Southampton (2010).
[58] W. Yan, L. Shi, Y. Kong, Y. Wang, H. Liu, J. Xu, S. Chen, L. Zhang, Z. Huang, S. Liu, and G. Zhang, J. Phys. D: Appl. Phys. **39**(19), 4245 (2006).
[59] S. Kim, V. Gopalan, K. Kitamura, and Y. Furukawa, J. Appl. Phys. **90**(6), 2949 (2001).
[60] O. F. Schirmer, O. Thiemann, and M. Wöhlecke, J. Phys. Chem. Solids **52**(1), 185 (1991).
[61] S. Chao and C. C. Hung, Appl. Phys. Lett. **69**(25), 3803 (1996).
[62] G. W. Ross, P. G. R. Smith, and R. W. Eason, Appl. Phys. Lett. **71**(3), 309 (1997).
[63] Y. J. Ying, C. L. Sones, H. Steigerwald, F. Johann, E. Soergel, K. Buse, R. W. Eason, and S. Mailis, in: Proceedings of CLEO/Europe-EQEC 2009, Munich, 2009.
[64] C. L. Sones, A. C. Muir, Y. J. Ying, S. Mailis, R. W. Eason, T. Jungk, A. Hoffmann, and E. Soergel, Appl. Phys. Lett. **92**(7), 072905 (2008).
[65] H. Steigerwald, M. Lilienblum, F. von Cube, Y. J. Ying, R. W. Eason, S. Mailis, B. Sturman, E. Soergel, and K. Buse, Phys. Rev. B **82**(21), 214105 (2010).
[66] S. Mailis, C. Riziotis, P. G. R. Smith, J. G. Scott, and R. W. Eason, Appl. Surf. Sci. **206**(1), 46 (2003).
[67] A. C. Muir, C. L. Sones, S. Mailis, R. W. Eason, T. Jungk, A. Hoffman, and E. Soergel, Opt. Express **16**(4), 2336 (2008).
[68] H. Steigerwald, Y. J. Ying, R. W. Eason, K. Buse, S. Mailis, and E. Soergel, Appl. Phys. Lett. **98**(6), 062902 (2011).
[69] S. Mailis, P. T. Brown, C. L. Sones, I. Zergioti, and R. W. Eason, Appl. Phys. A **74**(2), 135 (2002).
[70] P. T. Brown, S. Mailis, I. Zergioti, and R. W. Eason, Opt. Mater. **20**(2), 125 (2002).
[71] S. Mailis, C. L. Sones, J. G. Scott, and R. W. Eason, Appl. Surf. Sci. **247**(1–4), 497 (2005).
[72] C. L. Sones, C. E. Valdivia, J. G. Scott, S. Mailis, R. W. Eason, D. A. Scrymgeour, V. Gopalan, T. Jungk, and E. Soergel, Appl. Phys. B **80**(3), 341 (2005).
[73] V. Y. Shur, D. K. Kuznetsov, A. I. Lobov, E. V. Nikolaeva, M. A. Dolbilov, A. N. Orlov, and V. V. Osipov, Ferroelectrics **341**(1), 85 (2006).

[74] C. E. Valdivia, C. L. Sones, J. G. Scott, S. Mailis, R. W. Eason, D. A. Scrymgeour, V. Gopalan, T. Jungk, E. Soergel, and I. Clark, Appl. Phys. Lett. **86**(2), 022906 (2005).
[75] I. T. Wellington, C. E. Valdivia, T. J. Sono, C. L. Sones, S. Mailis, and R. W. Eason, Appl. Surf. Sci. **253**(9), 4215 (2007).
[76] V. Y. Shur, D. K. Kuznetsov, A. I. Lobov, D. V. Pelegov, E. V. Pelegova, V. V. Osipov, M. G. Ivanov, and A. N. Orlov, Phys. Solid State **50**(4), 717 (2008).
[77] D. K. Kuznetsov, V. Y. Shur, E. A. Mingaliev, S. A. Negashev, A. I. Lobov, E. L. Rumyantsev, and P. A. Novikov, Ferroelectrics **398**, 49 (2010).
[78] E. A. Mingaliev, V. Y. Shur, D. K. Kuznetsov, S. A. Negashev, and A. I. Lobov, Ferroelectrics **399**, 7 (2010).
[79] A. I. Lobov, V. Y. Shur, D. K. Kuznetsov, S. A. Negashev, D. V. Pelegov, E. I. Shishkin, and P. S. Zelenovskiy, Ferroelectrics **373**(1), 99 (2008).
[80] V. Bermúdez, L. Huang, D. Hui, S. Field, and E. Diéguez, Appl. Phys. A **70**(5), 591 (2000).
[81] A. Mehta, E. K. Chang, and D. M. Smyth, J. Mater. Res. **6**(4), 851 (1991).
[82] D. P. Birnie, J. Mater. Sci. **28**(2), 302 (1993).
[83] A. C. Muir, G. J. Daniell, C. P. Please, I. T. Wellington, S. Mailis, and R. W. Eason, Appl. Phys. A **83**(3), 389 (2006).
[84] U. Schlarb and K. Betzier, J. Appl. Phys. **73**(7), 3472 (1993).
[85] S. Mailis, C. Riziotis, I. T. Wellington, P. G. R. Smith, C. B. E. Gawith, and R. W. Eason, Opt. Lett. **28**(16), 1433 (2003).
[86] P. Ganguly, C. L. Sones, Y. J. Ying, H. Steigerwald, K. Buse, E. Soergel, R. W. Eason, and S. Mailis, J. Lightwave Technol. **27**(16), 3490 (2009).
[87] C. L. Sones, P. Ganguly, Y. J. Ying, F. Johann, E. Soergel, R. W. Eason, and S. Mailis, Opt. Express **17**(26), 23755 (2009).
[88] Y. S. Luh, R. S. Feigelson, M. M. Fejer, and R. L. Byer, Journal of Crystal Growth **78**(1), 135–143 (1986).
[89] F. Lacour, N. Courjal, M. P. Bernal, A. Sabac, C. Bainier, and M. Spajer, Opt. Mater. **27**(8), 1421 (2005).
[90] F. Sulser, G. Poberaj, M. Koechlin, and P. Günter, Opt. Express **17**(22), 20291 (2009).
[91] F. Chen, J. Appl. Phys. **106**(8), 081101 (2009).
[92] Z. Ren, P. J. Heard, J. M. Marshall, P. A. Thomas, and S. Yu, J. Appl. Phys. **103**(3), 034109 (2008).
[93] W. S. Yang, H. Y. Lee, W. K. Kim, and D. H. Yoon, Opt. Mater. **27**(10), 1642 (2005).
[94] I. E. Barry, G. W. Ross, P. G. R. Smith, R. W. Eason, and G. Cook, Mater. Lett. **37**(4–5), 246 (1998).
[95] I. E. Barry, PhD thesis, University of Southampton, Southampton (2000).
[96] R. W. Eason, I. E. Barry, G. W. Ross, and P. G. R. Smith, Electron. Lett. **35**(4), 328 (1999).
[97] I. E. Barry, G. W. Ross, P. G. R. Smith, and R. W. Eason, Appl. Phys. Lett. **74**(10), 1487 (1999).
[98] A. B. Randles, M. Esashi, and S. Tanaka, IEEE Trans. Ultrason. Ferroelectr. Freq. Control. **57**(11), 2372 (2010).
[99] R. V. Schmidt and I. P. Kaminow, Appl. Phys. Lett. **25**(8), 458 (1974).
[100] C. Y. J. Ying, G. S. Murugan, G. Brambilla, C. L. Sones, E. Soergel, J. S. Wilkinson, R. W. Eason, M. N. Zervas, and S. Mailis, in: Proceedings of CLEO/QELS 2011, Baltimore, 2011.
[101] C. Y. J. Ying, G. S. Murugan, G. Brambilla, C. L. Sones, E. Soergel, J. S. Wilkinson, R. W. Eason, M. N. Zervas, and S. Mailis, in: Proceedings of the Symposium on Photonics and Optoelectronics Conference (SOPO 2011), Wuhan, 2011.
[102] M. L. Gorodetsky, A. A. Savchenkov, and V. S. Ilchenko, Opt. Lett. **21**(7), 453 (1996).
[103] C. Y. J. Ying, C. L. Sones, A. C. Peacock, F. Johann, E. Soergel, R. W. Eason, M. N. Zervas, and S. Mailis, Opt. Express **18**(11), 11508 (2010).
[104] H. Hu, R. Ricken, W. Sohler, and R. B. Wehrspohn, IEEE Photonics Technol. Lett. **19**(6), 417 (2007).
[105] H. Hu, R. Ricken, and W. Sohler, Appl. Phys. B **98**(4), 677 (2010).
[106] L. Wang, J. H. Zhao, and G. Fu, J. Lightwave Technol. **28**(9), 1344 (2010).